Wolfgang Rao Bodlos, BSc

Surface Crystallization Studies of Decyl-Phenyl-Benzothieno-Benzothiophene

MASTER'S THESIS

to achieve the university degree of

Diplom-Ingenieur

Master’s degree programme: Advanced Materials Science

submitted to

Graz University of Technology

Supervisor

Ao.Univ.-Prof. Dipl.-Ing. Dr.techn. Roland Resel

Institute of Solid State Physics

Graz, November 2018

AFFIDAVIT

I declare that I have authored this thesis independently, that I have not used other than the declared sources/resources, and that I have explicitly indicated all material which has been quoted either literally or by content from the sources used. The text document uploaded to TUGRAZonline is identical to the present master‘s thesis.

Date

Signature

Acknowledgement

Foremost, I would like to thank my supervisor Roland Resel for the topic, the supervision and the continuous support. Secoundly my working group for creating a pleasant working environment and helping me with my progress. Namely Andreas Hofer, Benedikt Schrode, Sebastian Hofer and Stefan Pachmajer. Apart from my group I would like to thank all people from the Institute of Solid State Physics. Especially Birgit Kunert, Elisabeth Stern and Harald Kerschbaumer. Specifically related to my work I would like to thank Luca Beverina for providing the samples and Sebastian Hofer for helping me with the heating experiments and providing beautiful plots.

Abstract

Benzothieno[3,2-b][1]benzothiophene (BTBT) derivatives are very promising candidates in the field of solution processable organic semiconductors that could enable low-cost production of flexible and large-area electronics. BTBT derivatives have delivered some of the highest mobilities among organic semiconductors. Especially 2-decyl-7-phenyl-[1] benzothieno[3,2-b][1] benzothiophene (Ph-BTBT-10) drew attention after uniform and molecularly flat polycrystalline thin films were produced. In this work the surface crystallization behaviour of Ph-BTBT-10 is investigated together with its phase transitions during heating up to 240°C and cooling back. Thin films starting from the monolayer regime up to thick films were prepared by spin coating. The films were investigated in terms of crystalline properties and thin film morphology by X-ray diffraction, X-ray reflectivity and Grazing Incidence X-ray diffraction, atomic force microscopy and optical microscopy. It is shown that at the lowest concentration of 0.3 g/l an uncompleted monolayer of standing molecules with the aromatic core pointing towards the substrate is formed. At higher concentrations between 0.5 g/l and 3 g/l strong island growth starts which leads to the formation of macroscopic islands at the highest concentration of 5 g/l. The phase transition behavior at elevated temperatures was observed trough in-situ X-ray reflectivity measurements. The disappearance and shift of Bragg peaks during the transition into the crystal E phase and back to the bulk phase is demonstrated. Furthermore it is shown that at concentrations and spin speeds between 1.5 - 5 g/l and 1000 - 1600 rpm a disordered crystal E phase is formed under ambient conditions. This phase shows comparable Bragg peak positions as the crystal E phase above 149°C, however the peaks are much broader suggesting a disordered crystal E phase.

Kurzfassung

Benzothieno[3,2-b][1]benzothiophene (BTBT) Derivate zählen zu den vielversprechendsten organischen Halbleitern, die durch Ihre Verarbeitbarkeit in Lösung eine kostengünstige Produktion von flexibler und großflächiger Elektronik ermöglichen könnten. Dabei zeigen BTBT Derivate einige der höchsten Mobilitäten unter organischen Halbleitern. Von besonderem Interesse erscheint 2-decyl-7-phenyl-[1] benzothieno[3,2-b][1] benzothiophene (Ph-BTBT-10), nachdem uniforme, auf molekularer Ebene flache Dünnschichten des Moleküls produziert wurden. In dieser Arbeit wird das Oberflächen Kristallisatiozionsverhalten von Ph-BTBT-10 untersucht, sowie dessen Verhalten beim Erhitzen auf 240°C und nachfolgendem Abkühlen. Hierzu wurden Dünnschichten beginnend bei einer Monolayerstrucutre bis hinauf zu dicken Lagen über das Rotationsbeschichtungsverfahren hergestellt. Die Schichten wurden auf ihre kristallinen Eigenschaften sowie ihrer Oberflächen Morphologie mittels Röntgendiffraktometrie, Röntgenreflektometrie, Röntgendiffraktometrie mit streifendem Einfall, Rasterkraftmikroskopie und optischer Lichtmikroskopie untersucht. Es wird gezeigt, dass bei der niedrigsten Konzentration von 0.3 g/l eine unvollständige Monolage aus aufrecht stehenden Molekülen geformt wird, die mit dem aromatischen Kern zum Substrat zeigen. Bei höheren Konzentrationen zwischen 0.5 g/l und 3 g/l bilden sich Inselstrukturen, die bei der höchsten Konzentration von 5 g/l zu makroskopischen Kristalliten heranwachsen. Das Phasenübergangsverhalten bei erhöhten Temperaturen wurde mittels in situ Röntgenreflektometrie gemessen. Dabei wird das Verschwinden und Verschieben von Brugg-Peaks während des Übergangs in die

Crystal E Phase und zurück in die Bulk Phase detailliert aufgelöst. Weiters wird gezeigt, dass bei Konzentrationen und Umdrehungsgeschwindigkeiten zwischen 1.5 – 5 g/l und 1000-1600 rpm sich eine ungeordnete Crystal E Struktur unter atmospherischen Bedingungen bildet. Diese Phase zeigt vergleichbare Bragg-Peak Positionen wie die Crystal E Phase über 149°C. Sie sind aber breiter, was auf eine ungeordnete Crystal E structur hindeutet.

Contents

1 Theory and Fundamentals

1.1 Polymorphism

Polymorphism expresses the ability of a compound to adopt multiple packing states upon crystallization. It is prevalent among organic molecules which are characterized by weak Van der Waals and electrostatic "(i.e. quadrupole)" interactions. Different polymorphs of the same material often possess very distinct physical properties such as the solubility, melting point, optical, electronic, and mechanical properties. Especially the electronic properties are very sensitive to changes in molecular packing.[2] They can alter the π orbital overlap and thereby enhance charge transport significantly up to orders of magnitude.[4] This offers a very convenient way to optimize material performance without changing the chemical composition.[14] In fact, various benchmark organic semiconductors like pentacene, sexithiophene, rubene or BTBT derivatives are polymorphic. It is even assumed that around one-third of organic substances show polymorphism under normal pressure conditions.[30] In the context of organic electronics, especially OFETs, enhancing the electrical properties at surface or interface regions is of major interest. There the charge transport is localized to an area of a few molecular layers and is very dependent on their packing. At these boundaries different polymorphic forms often can appear. Substrate induced phases (SIP) rise from specific interactions between the molecule and the substrate and are not necessarily related to any matching of unit cells between film and substrate. They form a layer in the vicinity of the rigid substrate that can differ significantly in molecular packing from the bulk phase overhead as illustrated in figure 1.1. The first and most-investigated SIP is the thin-film phase of pentacene. The discovery was followed up by many other molecules exhibiting SIPs including the BTBT derivative C8O–BTBT–OC8. It is still not fully understood how SIPs originate. Limitations of the experimental techniques still leave open if both phases are always present from the first layer onwards or if the bulk phase only appear above a critical film thickness.[208] Other studies suggest that the different growth conditions are much more important than the thickness of the SIP film.[218] This includes the influence of the deposition method and the substrate properties.

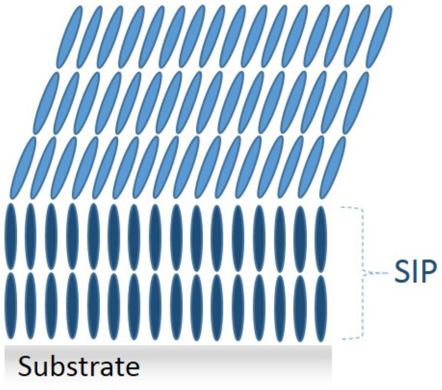

Figure 1.1: Schematic illustration of a Surface Induced Phase (SIP) at the bottom that has a different crystal structure than the bulk crystal structure growing on top.

1.2 The BTBT - Family and Ph-BTBT-10

The search for ideal solution-processable organic OFET materials became a field of intense research and has gained considerable industrial interest in recent decades. While a lot of attention was driven to π-conjugated polymers with aromatic and/or heteroaromatic backbones, represented by poly(3-hexylthiophene) (P3HT) their limitation became quickly clear. The device performance of polymeric materials is limited by the statistical distribution of the molecule size and their structural defects like mislinked monomers which can act as carrier traps in semiconducting channels.[7][11] Therefore the focus shifted towards small molecule organic semiconductors (OSCs) that have the advantages of a well-defined structure, being easily purifiable and having controllable properties.[7][11] However although tremendous progress in molecular design, processing and engineering has been achieved only a few molecules seem to be suitable. Besides the traditional issues of mobility and the resistance towards oxidation at ambient conditions the weakly van der Waals bounded systems need a preferential alignment along the highest charge transport axis to gain the full potential of single crystals.[27] To enhance the resistance at ambient conditions a very successful strategy among p-channel organic semiconductors became the reduction of the HOMO energy level (E_{Homo}), while still keeping the material suitable to hole injection from the electrode. Enhancing the mobility appeared more difficult and lead to the examination of many different molecules. Apparently π-extended heteroaromatics are most promising because they transport carriers by intermolecular orbital overlap.[1] Additionally heteroatoms inside the structure with larger radii than carbon, like sulfur, are expected to enhance the orbital overlap even more. Among the many reported molecular semiconductors that possess such a structure, [1]benzo-thieno[3,2- b]benzothiophene (BTBT) and dinaphtho[2,3-b:2,3-f]thieno[3,2-b]thiophene [27] have demonstrated some of the highest mobilities reported so far.[7][11][27].

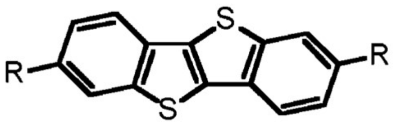

Figure 1.2: The chemical structure of the BTBT core. The aromatic core contains two sulfur atoms and can be extened at both side ends, forming its derivatives.[7]

The structure of BTBT is shown in figure 1.2. The structure of the molecule was proposed as early as 1949 and synthesized for the first time in the 1980s for the potential use as a liquid crystalline material. The first OFETs where fabricated with 2,7-diphenyl-BTBT (DPh-BTBT) in 2006.[29] One year later in 2007 field-effect mobilities higher than 1.0 $cm^2V^{-1}s^{-1}$ were reported for organic p-channel FET.[7][11]. Since then many BTBT derivatives have been synthesized and studied in the context of OFETs. [**?**][**?**] Indeed many of them show high mobilites and already found use in some sophisticated devices.[17][15] Recently it was shown that BTBT derivatives also show polymorphic phases at ambient conditions like $C8 - BTBT$ and $C8O - BTBT - OC8$. The latter even exhibits a metastable SIP. [13] Studies on 2-decyl-7-phenyl-[1] benzothieno[3,2-b][1] benzothiophene (Ph-BTBT-10) revealed that it transforms into a Crystal E phase at elevated temperatures. It was possible to produce uniform and molecularly flat polycrystalline thin films of this molecule that preserved their high thermal durability and mobility. [10] The Ph-BTBT-10 used in this experiments was synthesized by the Suzuki coupling reaction between 2-decyl-7-iodo-[1]benzothieno[3,2-b][1]benzothiophene(I-BTBT-10) and phenyl borate. The structure is shown in figure 1.3 together with its calculated HOMO and LUMO levels. It has a high semiconducting core with dislocated electrons at the left and the the long alkyl chain attachment at the right making it more solvent processable.

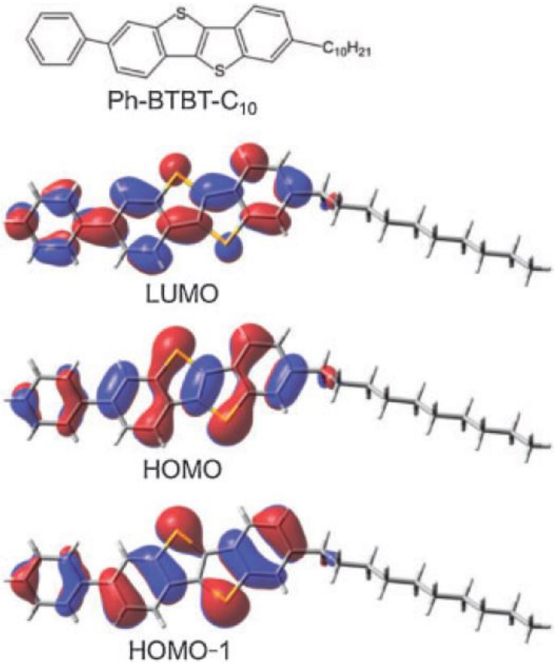

Figure 1.3: The chemical structure of Ph-BTBT-10 is shown on top. It consists of a BTBT core, connected to a phenyl group at the left side and with a decyl-chain at the right side. The HOMO and LUMO levels are illustrated underneath emphasizing the semiconductive structure.[19]

1.3 Liquid Crystal Phases of OFETs and the Crystal E Phase

There are various types of liquid crystal phases, also called mesophases, that are generally observed for molecules with highly anisotropic shapes. They have properties of both solids and liquids and posses long range orientational and/or positional order. LCs are mostly thermotropic and therefore only exist over certain temperature ranges. Calamitic LCs, which are rod-like molecules with cylindrical symmetry, can obtain a nematic (N) or smectic phase. Nematic phases have no positional order but an orientational order. Which is described by a vector, n, that indicates the preferred molecular orientation. Smectic LCs possess a higher degree of order namingly positional and orientational. Figure 1.4 shows the different smectic phases in comparison to a nematic phase.

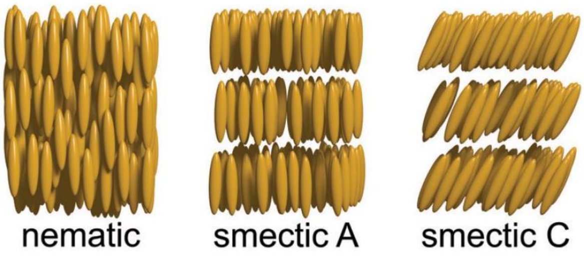

Figure 1.4: The classification of liquid crystals depending on their degree of order. Nematic liquid crystals with only orientational order (left) and smectic liquid crystals with orientational and one-dimensional positional order (center) that are independent of each other (right).[6]

The crystal E Phase is a smectic-like soft crystal phase often also called smectic E. It has long range positional order in which the molecules are arranged in such a way that their long axes are perpendicular to the layer planes. The arrangement is illustrated in Figure 1.5, a biaxial structure consisting of orthorhombically ordered arrays. It possesses a herringbone structure that hinders the molecules in undergoing complete rotational movement around their long axes. However, they undergo a rapid reorientation motion which is of an oscillatory nature. This movement can be imagined as a cooperative flapping around their long molecular axes. The crystal E Phase used to, and still often is called smectic E phase but was reconsidered to be a soft crystal phase due to long range transitional order. The solubility of organic semiconductors in organic solvents decreases considerably with the extension of the π-electron skeletons due to increasing cohesion. [22] Therefor they are mostly chemically modified by alkyl chain substitution to improve their solubility. This leads to a similar molecular design as in calamitic liquid crystalline materials. Thereby common OFET materials like the BTBT derivatives often adopt liquid crystalline phases at elevated temperature.

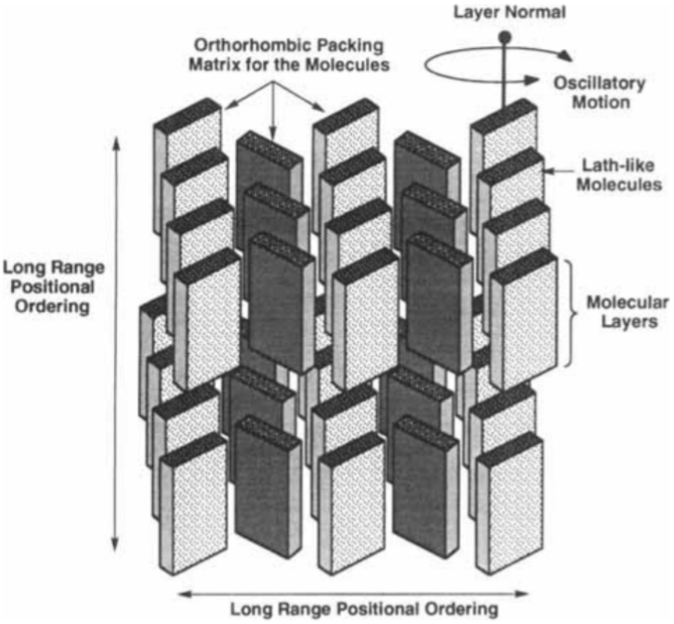

Figure 1.5: The structure of the crystal E phase with its herringbone arrangement for three molecule layers stacked upon each other.[3]

2 Experimental Methods

2.1 X-ray diffraction

When Max and Laue performed the first X-ray diffraction experiments in 1912 they already remarked the huge potential for crystallographic research. Indeed in the following century X-ray diffraction became the most convenient way to analyze the atomic and molecular structure of a crystalline materials. The wavelength of the X-rays is chosen between 0.5 and 2 angstrom which corresponds to the interatomic distance in crystals.[26] The waves that penetrate into the sample diffract from the electron clouds surrounding each individual Atom and interfere with each other strongly. The outcoming waves possess detailed information about the underlying periodicity of their scattering centers, hence the individual atoms of the crystal. When measuring the angular position versus intensity of the diffracted waves one can determine several material properties depending on the setup and X-ray technique. This includes information about the crystallinity, lattice structure, lattice defects, mosaicity, crystal size, microstrain and macrostrain. There are different measuring methods with distinct capabilities namingly single crystal diffraction, powder diffraction or small angle X-ray diffraction. In this work specular X-ray Diffraction (XRD) and Grazing Incidence X-ray diffraction (GIXD) where performed. The following chapter will describe the techniques and setups used and give a basic description.

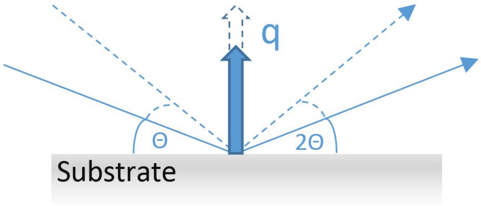

Figure 2.1: Illustration of how the q vector scales with the scattering angle 2θ during a specular X-ray diffraction measurement. It grows perpendicular to the surface with increasing angle.

2.2 Specular X-ray diffraction

In specular X-ray diffraction information perpendicular to the surface, so called out-of-plane information is obtained.[20] In terms of the incident and diffracted beam, both enclose the same angle with the substrate surface and lie in one plane, making the q vector normal to the substrate surface. Figure 2.1 illustrates how the q vector scales with 2Theta. As 2Theta increases q grows and as soon as it equals the interplanar distance of a plane a peak of intensity is measured.

$$q = \frac{4\pi}{\lambda} sin(\theta)$$

In figure 2.2 the measurement process is illustrated. By using the Bragg equation

$$n\lambda = 2d_{hkl} sin(\theta)$$

in which λ stands for the given wavelength, θ is half of the scattering angle 2θ and d_{hkl} is the interplanar spacing between lattice planes perpendicular to the surface. This relation connects the interplanar distance with the angle 2Theta. Furthermore investigating the width of the peaks and using the Scherrer equation one can derive the crystallite size and the strain in out-of-plane direction.

$$L(2\theta) = \frac{\lambda}{Bcos(\theta)}$$

with B being the peak width which is inversely proportional to the crystallite size L. [20] The measurements were performed with a PANalytical Empyrean shown in figure 2.3 The picture gives an overview of the X-ray diffractometer.

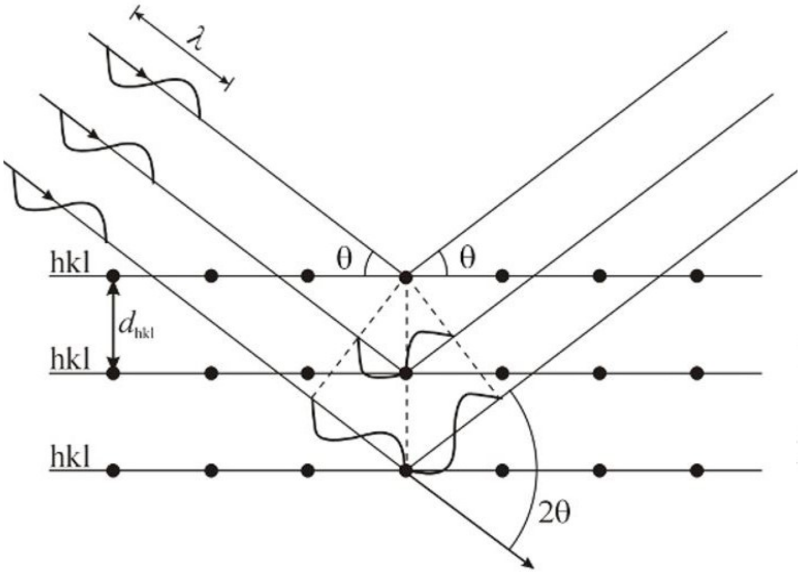

Figure 2.2: The measurement principle of specular X-ray diffraction. The geometry, the direction of propagation into and out of the sample, and the interference is schematically illustrated for a three layered sample with the interplanar distance of d_{hkl}.[8]

The left side moves on the θ circle while the right side does it on the 2θ circle. Starting from the left *(1)* the X-ray tube is shown, a water cooled copper tube powered with 40 mA at 40 kV. Moving to the right the incident beam optics *(2)* can be seen containing a 1/8° slit, a 10 mm mask and a parallel beam mirror. The mirror collimates the X-rays into a parallel beam with a divergence below

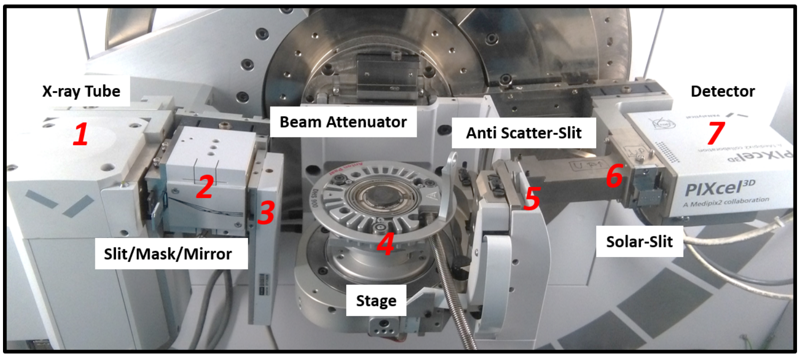

Figure 2.3: The PANalytical Empyrean diffractometer with its relevant components marked in red (1-7). The heating stage DHS 900 for temperature dependent investigations is mounted.

0.055° and serves as a monochromator to get mainly CuKα radiation that has a wavelength of λ = 0.154 nm. The beam then passes through a programmable beam attenuator *(3)* that inserts a 0.125 mm Ni-plate above a certain count rate to protect the detector. In the center lies the stage mounted onto a 3-axis cradle *(4)*. After interacting with the sample the diffracted X-rays pass through a 7.5 mm anti-scatter slit *(5)* and a 0.02 rad Soller slit *(6)* before finally arriving at the detector *(7)*. The PIXcel3D detector is a solid state detector with 255x255 pixels of 55x55 μm size. It can be switched between three different modes. In our measurements the so called 1D-Mode for specular diffraction or receiving slit mode was used in which the detector acts like a point detector.

2.3 X-ray Reflectivity

X-ray reflectivity (XRR) is a surface sensitive thin film characterization method that measures reflection intensity curves to deliver detailed information about the film. As for specular X-ray diffraction the measurements are performed specularly and therefor out of plane. However the angle of incidence is far smaller between 0° and 6° . The X-rays progress from a medium with higher index of refraction (air or N_2 gas) into a medium with lower index of refraction (Ph-BTBT-10 thin film) there is a critical angle in this range below which the beam is totally reflected off the surface. This is described by the refractive index of X-rays written [25][9]

$$n = 1 - \delta + i\beta$$

with a dispersion term

$$\delta = \frac{\lambda^2}{2\pi} r_e \rho_e = \frac{\lambda^2}{2\pi} r_e N_a \rho \frac{Z + f'}{A}$$

and an absorption term β

$$\beta = \frac{\lambda}{4\pi} \mu_x = \delta \frac{f''}{Z + f'}$$

where r_e is the electron radius, ρ_e is the electron density, μ_e is the linear absorption coefficient N_a the Avogadro Number, A the atomic mass, ρ the mass density and Z the number of electrons per atom. Z can be expanded by an atomic form factor $f' + if''$ due to dispersion and absorption. The critical angle is then expressed and related to δ by

$$\alpha_c = \sqrt{2\delta}$$

[18] Above the critical angle the X-rays start to transmit into the sample. If the thin film consists of multiple layers with different electron densities, the transmitted waves propagate to the next inferface layer and are again reflected and/or transmitted. This continues until the bare substrate is reached. All the reflected beams from the individual layers interfere with each other and behave like a Fabry Perot interferometer. If the thickness and electron density of the layers remain more or less constant and only the incident angle is varied the measurement signal should periodically increase and decrease. Figure 2.4 shows such an XRR curve of MoO3.

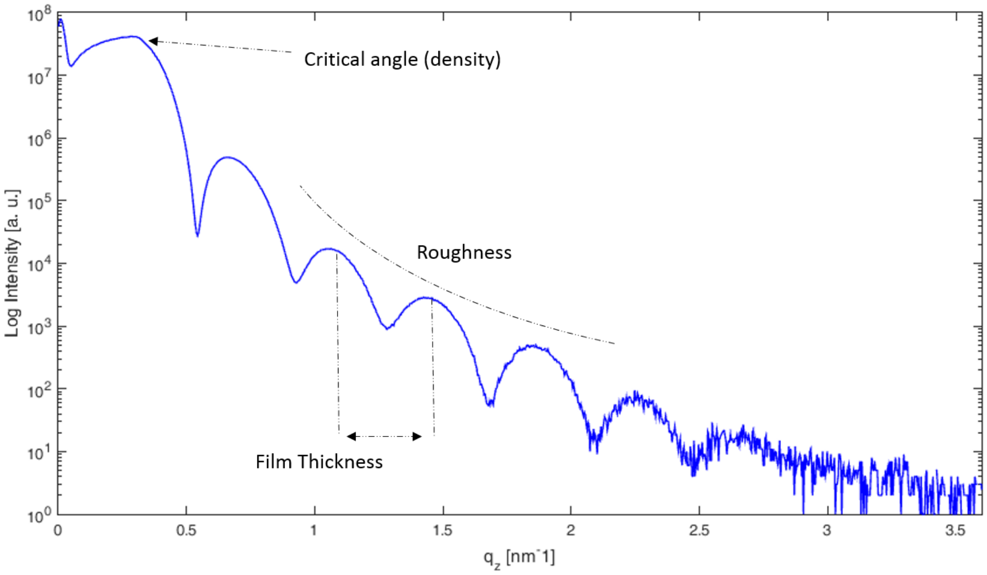

Figure 2.4: A X-ray Reflectivity measurement of MoO3 with all the important curve features pointed out. The point at which the intensity drops, the strength of the slope and the width of the Kiessig fringes.

From this measurement three parameters can be derived, the electron density related to the position of the critical angle, the film thickness from the width of the Kiessig fringes and the roughness from the slope of the curve. The latter occurs due to increased diffuse scattering with more surface roughness. [16] The thickness t of the film is related to the period of the finges by following relation

$$t \sim \frac{\lambda}{2\Delta\alpha}$$

with $\Delta\alpha$ standing for the fringe spacing. The parameters are extracted by fitting the curves. Most fitting routines use the Parratt formalism [23]. For the XRR measurements the same instrument and setup was used as for the specular X-ray diffraction shown in Figure 2.3. Thus, the 1/8° Soller slit *(2)* was swapped by a 1/32° one and the 7.5 mm anti scatter slit *(5)* was exchanged by a 0.1 mm one. The detector was switched to the 0D receiving slit mode using three open channels.

2.4 Grazing incidence X-ray diffraction (GIXD)

GIXD is a surface sensitive X-ray diffraction technique that has the capability of analysing the in-plane structure of thin film. This unique technique uses high intensity synchrotron radiation that strikes the sample surface at an angle below the point of total reflection. The main beam gets reflected of the surface but creates an evanescent wave that oscillates at the surface and decays exponentially into the thin film.[39] It diffracts from planes parallel and non-parallel to the surface and thereby gives detailed in-plain information. Figure 2.5 shows the diffraction geometry.

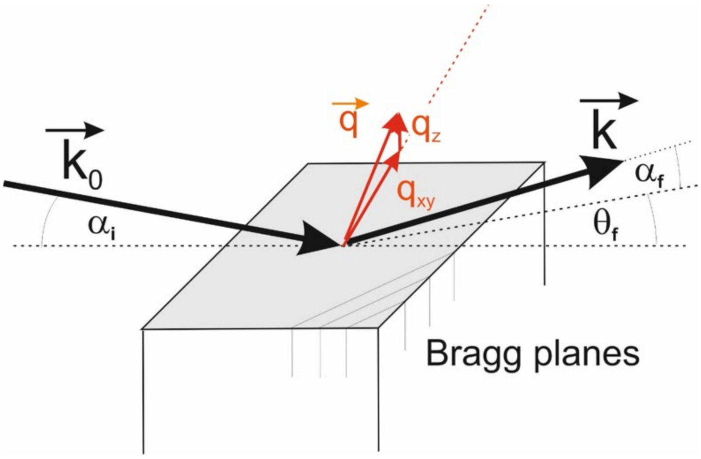

Figure 2.5: The diffraction geometry of GIXD. The q vector is tilted around the normal axis of the substrate during the measurment, obtain different q_{xy} components. This allows the measurment of Bragg planes of non perpendicular to the surfac as illustrated.

In terms of the q Vector it is not only skaled but also tilted due to changes of the q_xy component. The measurements were performed at the Synchrotron Elettra in Trieste at the X-ray Diffraction 1 (XRD1) beamline. The beamline consists of four components, the photon source, the beam optics, the sample stage and the detector. The photon source is a multipole wiggler with a range between 4 to 21 keV. The optics are formed by three elements. A cylindrical collimating mirror with a 50 nm Pt-coating, double-crystal Si(111) monochromator and a bendable toroidal focusing mirror with 50 nm Pt-coating. The sample stage is mounted on a Huber Kappa Goniometer. The detector is a Dectris Pilatus 2M. It uses a CMOS hybrid-pixel technology and was operated in the single-photon-counting mode. The amount of pixels are 1475 x 1679 = 2476525 of which each has a size of 172x172 μm^2.

2.5 Spin Coating

Spin Coating is a widely popular thin film production technique in which the substrate is rotated whereby the solution containing the material is spread over the surface. Centrifugal forces induce and dominate movement of the solution and thereby invoke processes far from thermodynamic equilibrium.[12] The spin speed of the solvent, the spin time, the viscosity of the solution and its evaporation rate are four values that determine the film properties. With increasing spin speeds the film thickness decreases due to stronger centrifugal forces associated with the rotary motion.[33] It creates more liquid outflow and strong airstreams that lead to fast drying times. With increasing viscosity, the film thickness grows as well. The viscosity and the evaporation rate of the solvent have a reciprocal relationship towards the film thickness. If one of both dominates the film thinning, the other plays an insignificant role. This already implies the common understanding of the film thinning mechanism during spin coating today, that it is a combined result of the convective radial outflow and the solvent evaporation.[33] Figure 2.6 shows a two stage model in which firstly both effects dominate and afterwards only the latter. The velocity gradient during radial outflow is illustrated in figure 2.6 (a) and approaches zero towards the surface. When compared to other deposition techniques spin-coating leads to a weaker structural quality and induces more structural defects. This is especially valid for small molecule OFETs which require time to self-assemble and/or crystallise.[12] Nevertheless the simplicity and the relative ease with which this technique can be set up, coupled with the thin and uniform coating that are achievable make it to a good starting point and benchmark.

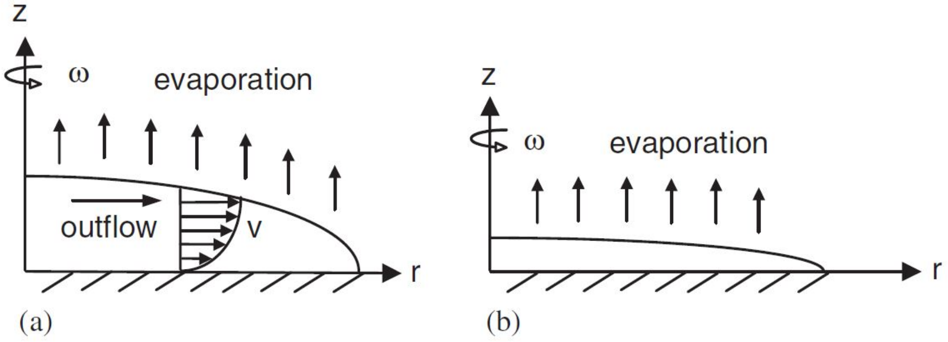

Figure 2.6: The liquid thinning process during spin-coating: a) first stage, convective radial outflow and evaporation cause the film thinning b.) second stage, the evaporation rate dominates the film thinning.[33]

2.6 Atomic Force Microscopy

An Atomic Force Microscope (AFM) is a high-resolution type of scanning probe microscope. Its main component is a microfabricated cantilever that senses the surface by approaching or touching it while oscillating at a high frequency. The cantilevers has a typical lateral dimensions of about 100μm, a thickness of 1μm, a spring constant between 0.1–1 Nm and a resonance frequencies between 50 and 800 kHz . Figure 2.7 shows a illustration of a AFM. To measure the elongation of the cantilever as precise as possible a laser beam is used. The beam is reflected off from the backside of the tip and is measured at a position sensitive detector. The exact distance of the tip above the sample surface depends on the operation mode and the size of the features. It varies between 0-10 nm, has a minimum at the contact mode and increases with the tapping and non-contact mode. In the latter Van der Waals forces dominate. They interact with the cantilever and deliver detailed topographic and phase information without damaging the sample surface. The topographic information gives detailed insight to the surface morphology while the phase information allows the distinction between different sample regions based on the surface stiffness/softness and adhesion towards the tip.

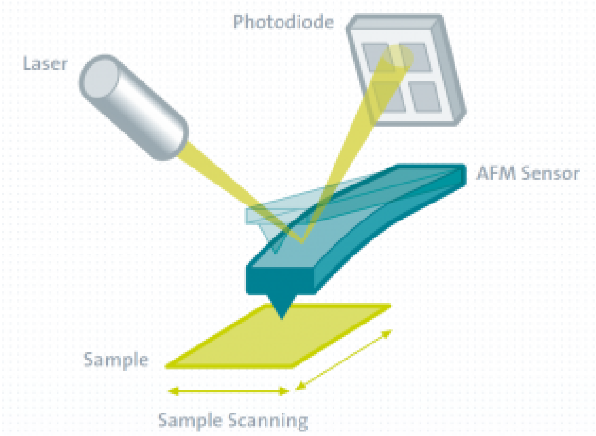

Figure 2.7: The Setup of a Atomic Force Microscope, with the cantilever, laser and photodetector illustrated.

2.7 Heating Stage DHS 900

The DHS 900 is a domed heating stage for non-ambient in-situ X-ray diffraction studies. The system is heatable up to 900°C and is shown in Figure 2.8. It possesses a dome to establish a protective atmosphere against oxidation or other chemical reactions of the sample at high temperatures. There are two diffent dome types that can be used, one made of PEEK, a synthetic material based on polyetheretherketone resin and the other out of graphane. The temperature is constantly measured by a thermocouple right underneath the sample which is connected to a high-end temperature control unit. Above 200° a cooling system consisting of a compressed air shower avoids any heat transfer to the goniometer. The heating-stage on the other hand possess a high thermal conductivity and chemical resistance which is achieved by using INCONEL, a austenitic nickel-chromium-based superalloy.

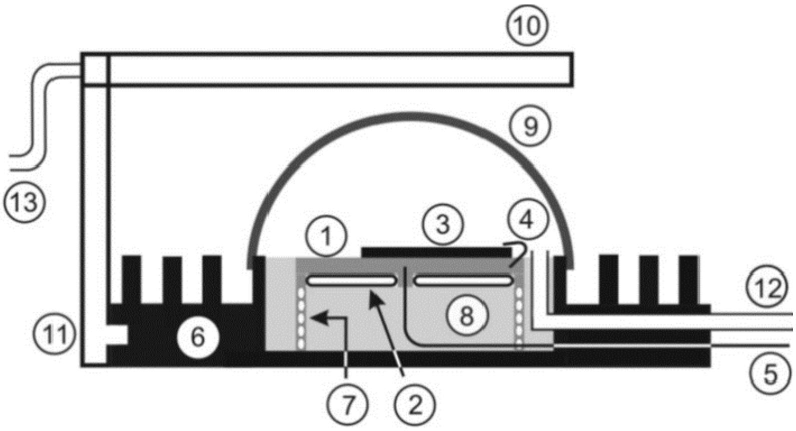

Figure 2.8: A schematic drawing of the DHS 900 heating-stage is shown. Its denoted parts are: heating plate (1), heating wire (2), sample (3), clamps (4), thermocouple (5), chassis (6), support of the heating plate (7), foamed Al_2O_3 (8), dome (9), emission rod (10), rotatable mounting of the cooling system (11), supply hose (12), air-pressure hose (13).[24]

3 Results and Discussion

3.1 Samples

The samples were prepared on and 20x20 mm^2 silicon wafers with a thermal SiO2 layers of 150 nm at the surface. They are from "Siegert Wafer GmbH" and were coated with a 2 nm organic protection layer after production. To remove this layer and avoid other impurities the substrates were cleaned in four steps. First by wiping with a lint-free tissue soaked in acetone. Then by treatment in a ultrasonic bath for 15 minutes while being placed in a beaker filled with acetone. After drying they were again wiped with a lint-free tissue but this time soaked in 2-Propanol. And finally they were again treated in a ultrasonic bath for 15 minutes with 2-Propanol. The ultrasonic bath is a Transsonic T310/H from Elma GmbH. Figure 3.1 shows the XRR signal of a cleaned substrate. The small Kiessig fringes correspond to the SiO2 layer. It has no measurable residues. During the spinning process heavy crystallization takes place at the edge of the substrates because the solution is held back before splashing off. This behavior at the edges is shown in figure 3.2. To control the film thinning better a small edge to surface ratio is desirable. Therefor 20x20 mm^2 substrates were used for this work.

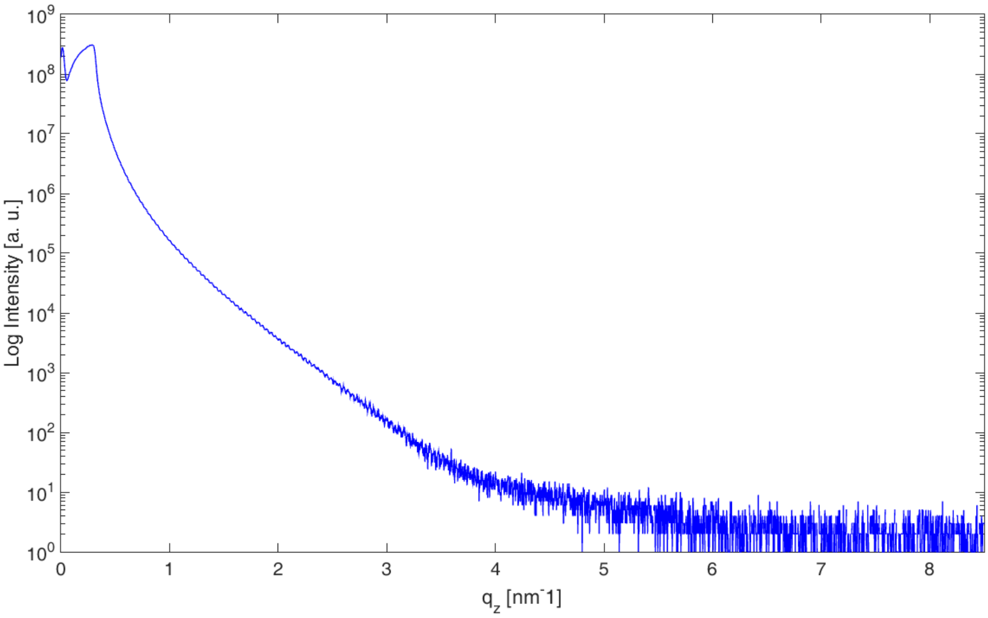

Figure 3.1: The XRR measurement of a cleaned sample showing small Kiessig fringes corresponding to the SiO2 surface layer.

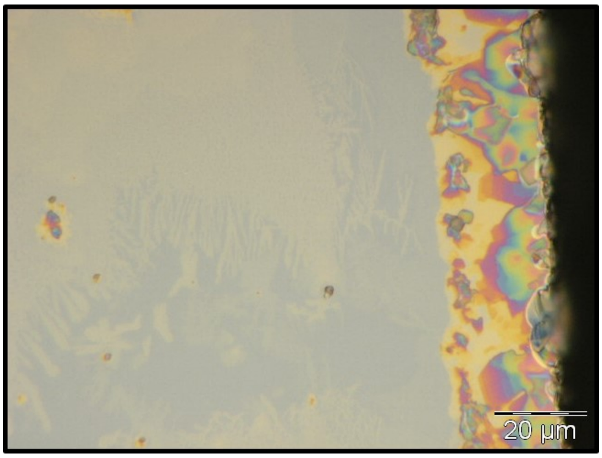

Figure 3.2: The edge area of a sample spincoated with the highest concentration of 5 g/l . A strong aggregation of Ph-BTBT-10 material is observed at the edges.

The Ph-BTBT-10 used in this experiment was obtained from the department of materials science of the University of Milano-Bicocca in Italy and came in a dry crystalline powder from. To prepare a spin coatable solution the material was dissolved in an organic solvent. In our case we chose toluene and p-xylene. Their molecular structures are shown in figure 3.3.

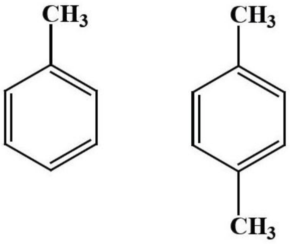

Figure 3.3: The molecular structure of Toluene (left) and p-Xylene (right). Both show a aromatic core connected to one or two methyl groups. Xylene is in the para configuration at which both methyl groups take apposing positions at the ring.[31]

Two samples with approximately the same concentrations of 1.2 g/l were prepared to compare the film formation with each other. Figure 3.4 shows the X-ray reflectivity measurements for both samples.

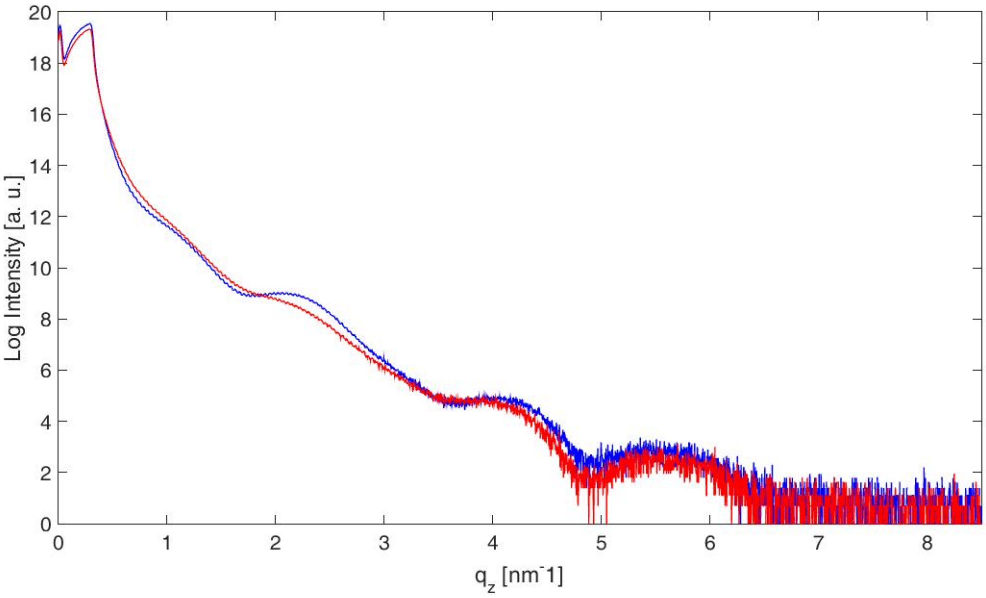

Figure 3.4: X-ray reflectivity measurements of two samples spin coated with Toluene (blue) and p-Xylene (red) at a concentration of 1.2 g/l.

The difference is small leading to the conclusion that the film formation is very similar in respect to Ph-BTBT-10. The experiments were therefore continued with Toluene only. The respective amount of Ph-BTBT-10 for each desired concentration was dissolved in 2 ml of solution. Unfortunately the solubility of the powder is rather poor and worsens with increasing concentrations due to clumping. Yet a proper dissolution was obtained using a half centimeter long magnetic stirring bar combined with a heating plate at a temperature between $50° - 70°C$. The ideal amount of solution was obtained by comparing results between $180\mu l$ and 250 μl. In figure 3.5 three XRR measurements of samples spin coated with the same concentrations but with different amounts of solutions are shown.

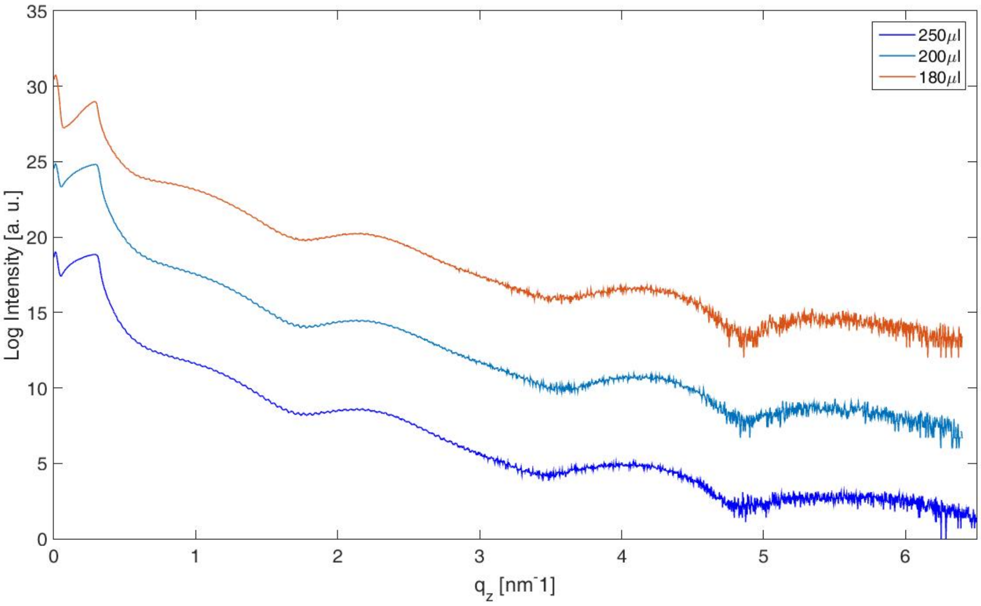

Figure 3.5: X-ray reflectivity measurements for different solution amounts of 180μl, 200μl und 250 μl used while spincoating. The curves are vertically shifted.

Because the difference is negligible 180μl was chosen for the study. The solution was vacuumed with a micropipet from each particular flask and deposited into the center of the substrate before spin coating. The spincoater is from Chemat Technology Inc. The spinning time was kept constant at 60 seconds to provide sufficient drying time. The individual samples were spin coated at spin speeds between 750 rpm and 2000 rpm. Above 2000 rpm the thinning of the film became too strong.

3.2 Monomolecular Layers

The samples that were spin coated with the lowest concentration of 0.3 g/l show no coverage visible with the free eye. When observed with a optical light microscope at a magnification of x1000 small rod like structures can be spotted demonstrated in figure 3.6.

Figure 3.6: Optical light microscope picture of a 0.3 g/l sample at a magnification of x1000 showing several micrometer long rods and a clear background.

Apart from the rods no surface structures are apparent with the optical microscope. To gain further insight to the features in between the rods AFM measurements were performed. Figure 3.7 (left) illustrates such a measurement showing that a typical dewetting structure is formed. The islands have a size of several micrometers and reach a surface coverage of about 40% as indicated in the upper right corner of the image. Figure 3.7 (right) shows the phase contrast image of the same measurement. The phase contrast towards the background is not very high, though observable. It suggests that we see the

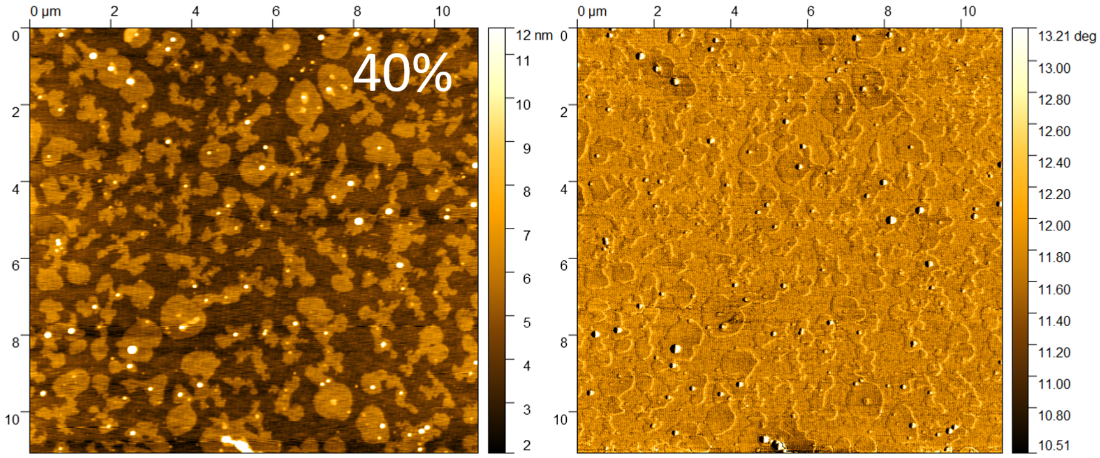

Figure 3.7: AFM measurement of a sample spin coated with a concentration of 0.3 g/l. Several micrometer big islands are spread over the surface leading to a coverage of 40%.

substrate in the background and on top the dewetting structure from spin coating. The height distribution of the picture is shown in figure 3.8. It has two peaks, the first (left) representing the average substrate height and the second (right) the average height of the highest layer. The difference between both is the island height which is about 1.7 nm. This appears to be lower than the long molecular axis length of the molecule but still far bigger than the short axis length. X-ray reflectivity measurements however contradict the AFM observation. Figure 3.9 shows the XRR curves for different spin speeds between 750 rpm and 2000 rpm. While at the lowest spin speed the curve divers from the others strongly, the increase in spin speed from 1000 rpm upwards doesn't seem to have a significant effect.

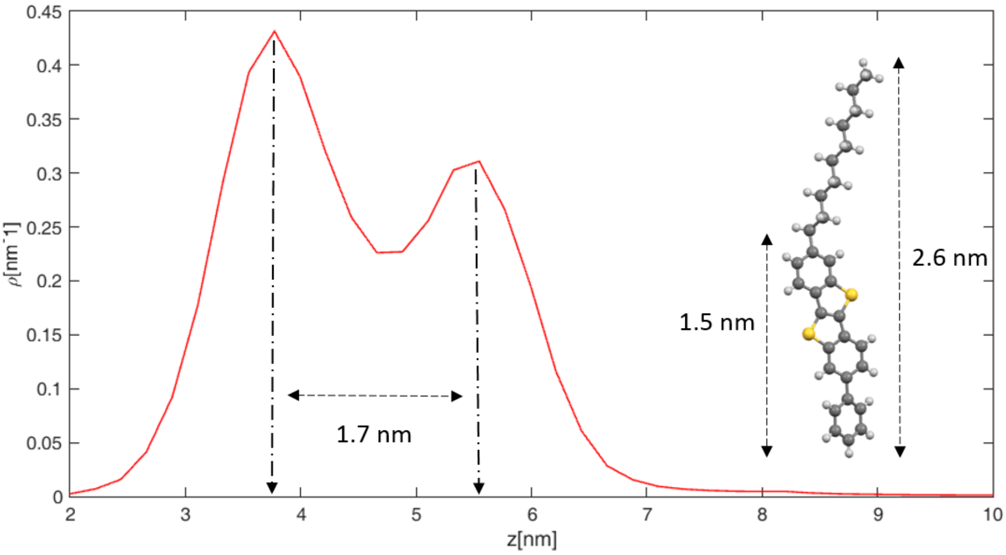

Figure 3.8: The height distribution of the AFM picture shown in figure 3.7. Two peaks are visible, the first (left) corresponding to the average substrate height and the second (right) to the average height of the islands. Next to the curve the molecule is shown to compare its length with the measurement.

The small Kiessig fringes correspond to the silicon dioxide layer with a thickness of 160 nm. The big fringes are best visible for 750 rpm but can also be spotted at higher spin speeds. To obtain valuable information from the curves they were fitted. The main fitting parameters were the number of layers their thicknesses and densities. The best results were obtained when splitting the molecule into two layers, one of high density representing the aromatic core and one of low density representing the alkyl chains. Figure 3.10 shows the fitting curves which suit the data very well (top) and the used model (bottom). According to the fit the total height as a sum of both layers is between 3.16 nm and 3.13 nm which is slightly higher but comparable to the long axis molecular length as illustrated next to the table with a standing molecule. This contradicts the AFM height measurements as mentioned ahead

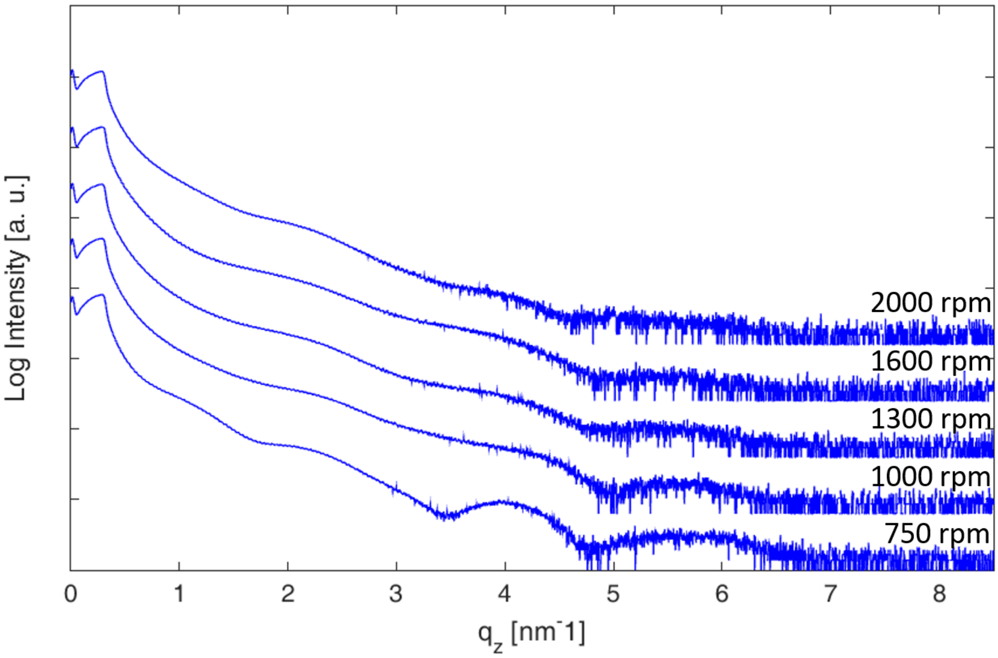

Figure 3.9: X-ray reflectivity measurements of samples spin coated with a concentration of 0.3 g/l at spin speeds between 750 and 2000 rpm.

and shown in figure 3.8. Previous studies on sub-monolayer structures of pentacene have already shown similar results with the X-ray reflectivity and AFM measurements possessing a systematic variation with respect to the measured island heights.[32] This can be explained by a difference in cantilever-surface interaction when passing from the stiff substrate to the softer organic film. The density values of the layers shown in figure 3.10 (bottom left) are lower than the presumption of about 1.7 g/cm^3 for the aromatic core and around 1 g/cm^3 for the alkyl chain. This is explainable by the low coverage of the dewetting structure visible in the AFM picture in figure 3.7 above. When multiplying the coverage of 40% to the expected densities of 1.4 g/cm^3 and 1 g/cm^3 we get 0.56 g/cm^3 and 0.40 g/cm^3 which is close to the values of the fit given in 3.10 (bottom left).

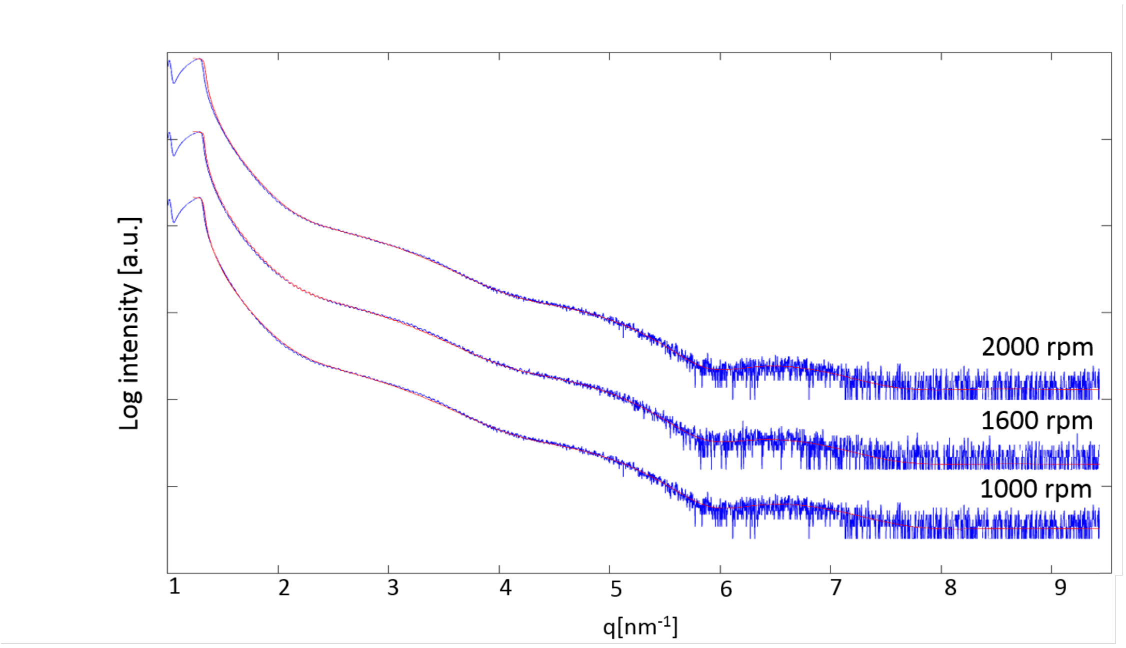

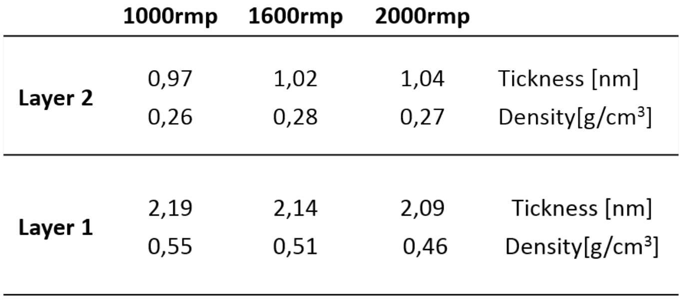

	1000rmp	1600rmp	2000rmp	
Layer 2	0,97	1,02	1,04	Tickness [nm]
	0,26	0,28	0,27	Density[g/cm^3]
Layer 1	2,19	2,14	2,09	Tickness [nm]
	0,55	0,51	0,46	Density[g/cm^3]

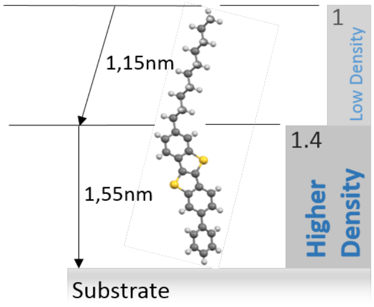

Figure 3.10: X-ray reflectivity measurements for 1000, 1600 and 2000 rpm together with their fitting curves (red), showing a strong overlap of the data with the fits. (top) The fitting parameters are given (bottom left) together with a illustration of how the molecule stands on the substrate (bottom right).

From the atomic force microscopy measurements it is non-apparent which orientation the molecules take towards the substrate surface. This is clearer when looking at the XRR fit parameters in figure 3.10 (bottom left). The more dense layer representing the aromatic core is for all measurements at the bottom by the substrate surface and the less dense layer representing the alkyl chains is on top. This suggests that the molecules stand on the surface as in figure figure 3.10 (bottom right). Therefore it can be concluded that the aromatic cores seem to prefer to interact with the substrate

3.3 Multilayers and Island Growth

When increasing the concentration to 0.5 g/l two different behaviour where observed. Firstly the coverage of the dewetting structure can increase without significantly changing the surface structure as shown in figure 3.11 (left). The coverage increases to about 68%. Its height distribution is illustrated in figure 3.11 (right). indicating a island height of 1.8 nm. This is similar to the observations at 0.3 g/l.

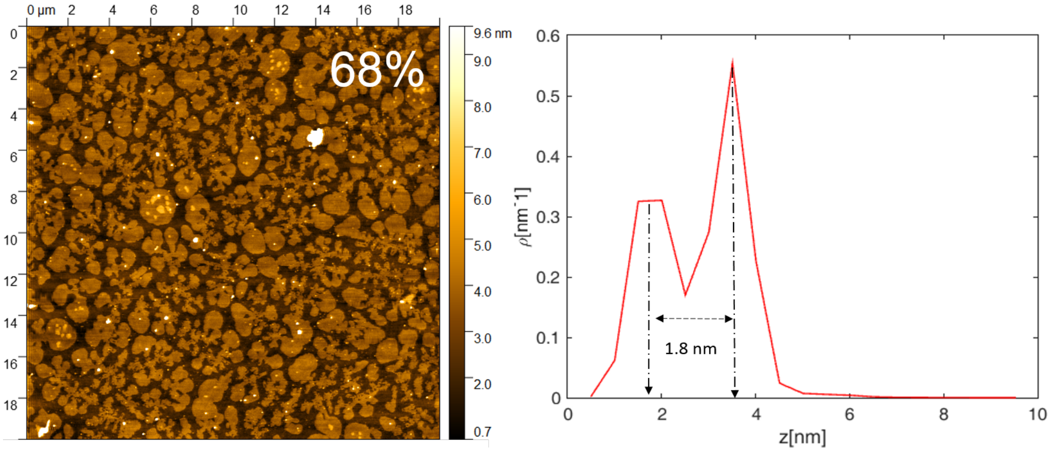

Figure 3.11: AFM picture of a sample spin coated with a concentration of 0.5 g/l showing a dewetting structure with a coverage of 68% (left). The height distribution of the measurement (right) with its corresponding peaks.

Secondly the morphology can change strongly like for most prepared samples at a concentration of 0.5 g/l. Figure 3.12 illustrates how several micrometer big islands form that are connected to each other by dendritic rods. The coverage remains around 60%. The islands that are distributed over the surface grow step wise after the first layer with the molecular long axis length as shown in figure 3.13.

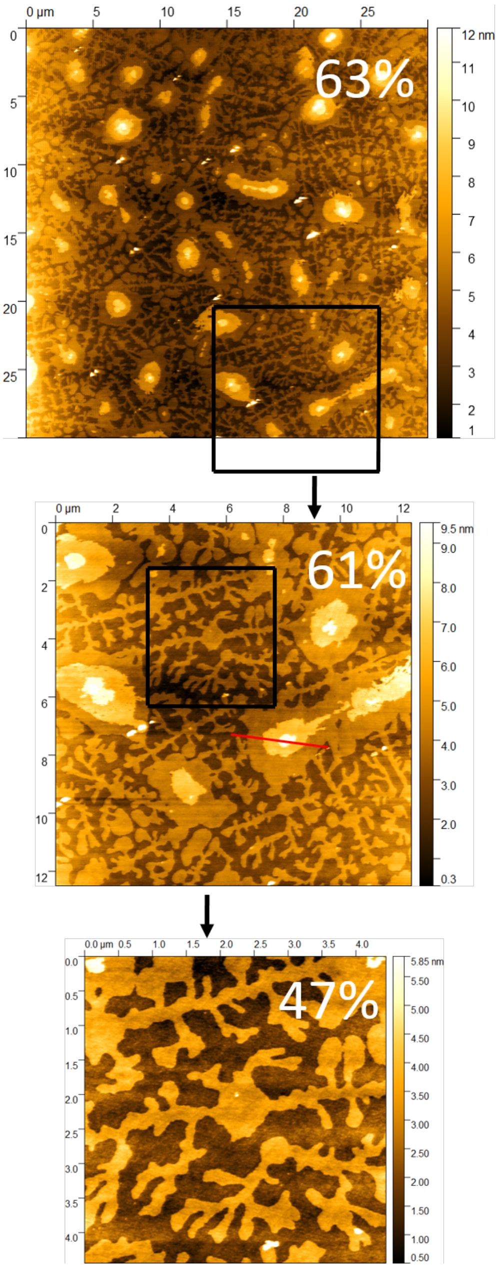

Figure 3.12: AFM pictures of a sample spin coated with a concentration of 0.5 g/l showing a dendritic structure with islands growing overhead. From the top image towards the bottom image the magnification increases.

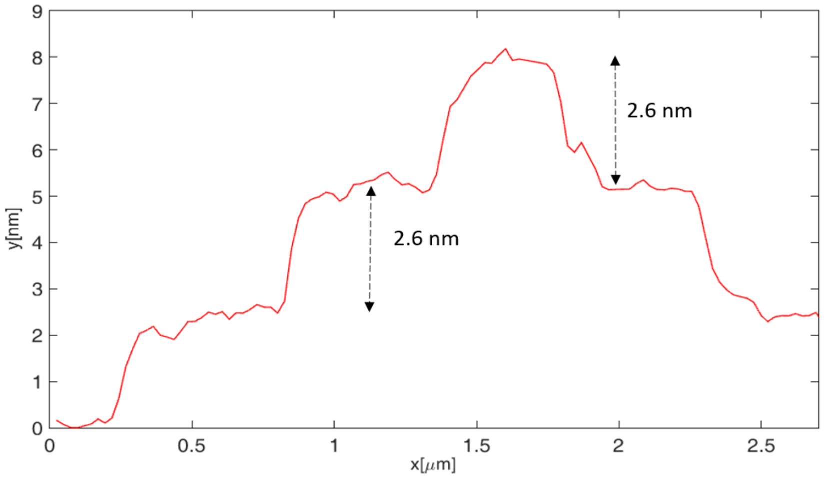

Figure 3.13: The height distribution of the island indicated with the red line in figure 3.12 (center). It grows with a terrace step height of 2.6 nm.

This clearly indicates that the molecules stand upright and stack onto each other vertically. During the island growth there seems to be a critical lateral diameter between 1 and 2 μm at which another layer starts to grow overhead. In figure 3.12 not more then three layers where observed. The dendrites in between the islands are several micrometers long, and connect the islands with each other. Their lateral width is below 0.5 μm. They possess a strong phase contrast towards the background as visible in figure 3.14 (right). This confirms that we are observing the most bottom layer with the substrate as the background. The height of the dendrites is illustrated in figure 3.14 (left).

The first peak corresponds to the average height of the substrate while the second peak relates to the molecular layer on top. The difference is the dendrite height 1.6 nm. This is comparable to the heights observed for the dewetting structures at 0.3 g/l and 0.5 g/l shown above in figure 3.8 and figure 3.11. It is again smaller than a upright standing molecule. This can be explained in two ways. By relating it to a systematic variation of XRR and AFM measurement

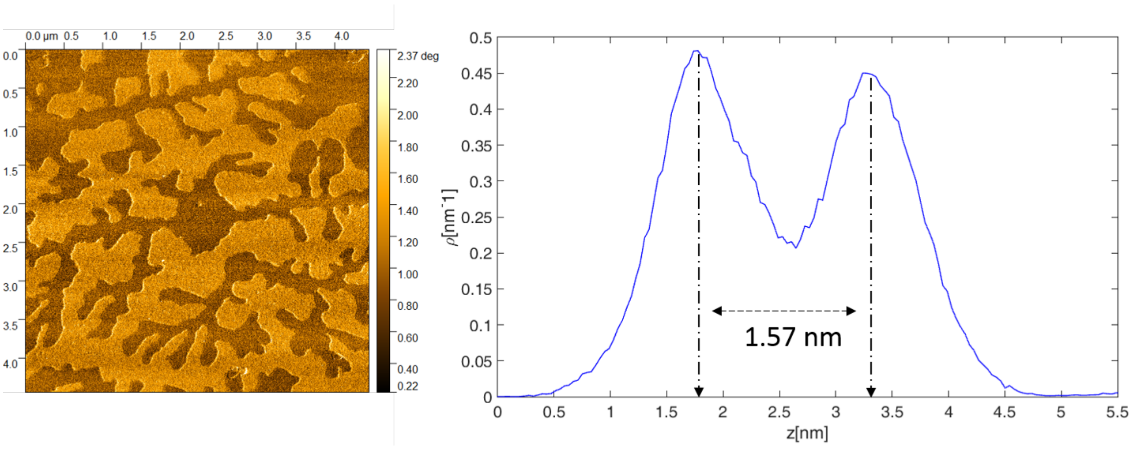

Figure 3.14: The height distribution of the magnified picture in figure 3.12 (bottom) together with the phase contrast image (left).

that only occurs at the most bottom layer by the substrate.[32] Or by assuming a specific interaction between the substrate and the molecule that reduces the layer height in comparison to the layers growing overhead that only interact with themselves. Unfortunately due to the non homogeneous growth of the layers, fitting and interpreting the X-ray reflectivity measurements becomes significantly harder. The XRR data with the fits is shown in figure 3.18 for spin speeds between 1000 and 2000 rpm. The model that works best has four layers representing two molecules that are split into a lower dense and a higher dense part respectively. At the first look the fitting curves match the data quit well.

The exact fitting parameters for each layer are shown in figure 3.16 together with a graph that illustrates the density values and total lengths with arrows of different color shading. The total length of all layers is between 5.7 nm and 5.9 nm which is only slightly above the length of two molecules stacked upon each other. However layer three approaches zero density. A layer with no density doesn't make physical sense, nevertheless there is a study from 2014

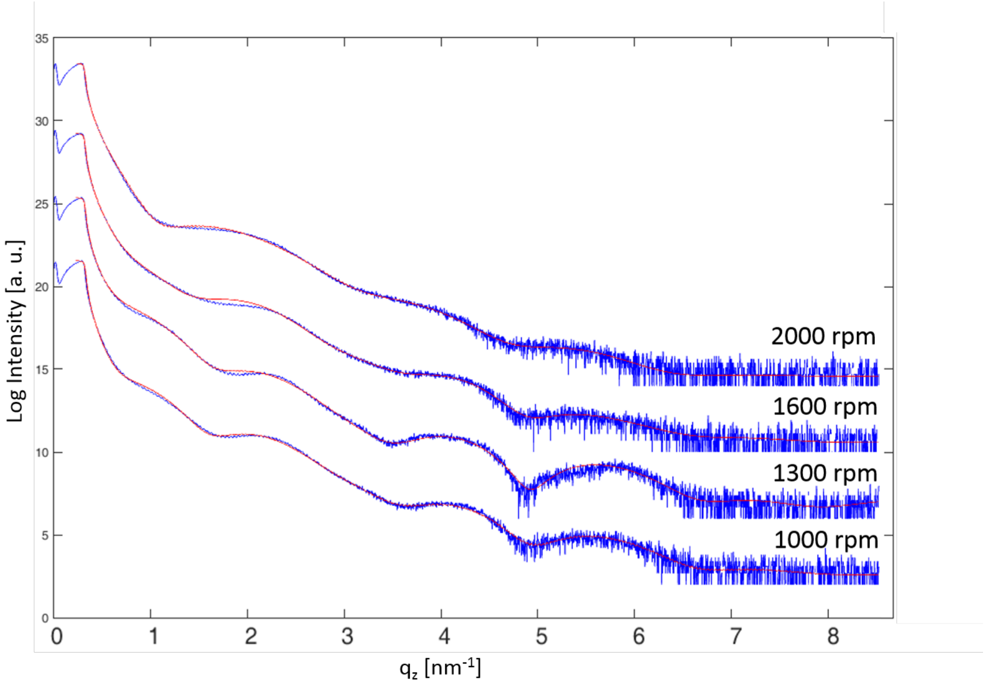

Figure 3.15: X-ray reflectivity measurements of samples spin coated with a concentration of 0.5 g/l. The curves represent different spin speeds between 1000 and 2000 rpm and are illustrated together with their fits (red).

showing that the introduction of a reduced density layer improves the XRR-fit of a Si-SiO2 system significantly.[28] At 2000 rpm the data resembles more the XRR curves of the monolayer structure at 0.3 g/l. This is in accordance to spin coating theory that assumes that the film thickness decreases with increasing spin speeds due to greater convective radial outflow of the solution. The best model for this curve consists of three layers and has a total length of 3.3 nm. For all spin speeds the fitting models indicate that the lower dense alkyl chain is at the most bottom layer by the substrate as shown in figure 3.16. This suggests that the molecules change their orientation when beginning to form multiple layers. This could occur due to preferential forces with the newly introduced overhead molecule layer.

	1000rmp	1300rmp	1600rmp	2000rmp
Layer 4	1,90 0,41	1,86 0,40	2,07 0,20	-
Layer 3	0,49 0	0,12 0	0,75 0	0,70 0,22
Layer 2	1,73 0,77	1,94 0,40	1,69 0,70	1,36 0,79
Layer 1	1,56 0,57	1,74 0,24	1,36 0,48	1,30 0,61

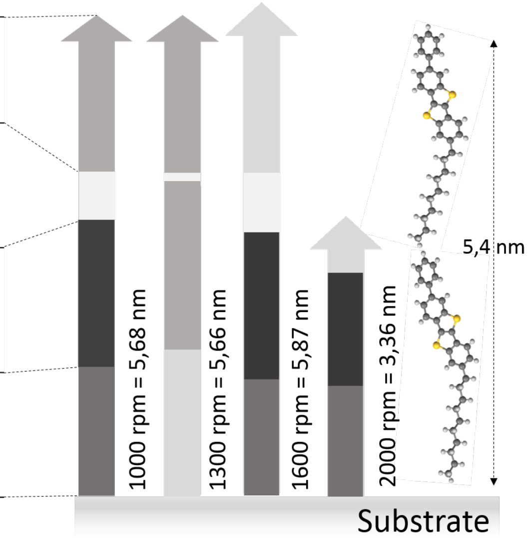

Figure 3.16: The table (left) shows the X-ray reflectivity fit parameters for the four layer model used to obtain the (red) curves in figure 3.18 for each individual spin speed. A illustration of the density distribution and total length of each fit is given by each respective arrow (right).

At higher concentrations of 0.7 g/l the structure changes noteable. Figure 3.17 shows the surface morphology observed with the AFM. The islands get bigger and reach a diameter of several micrometers. The dendrites broaden and partly interpenatrate into each other. The islands start to dominate the picture. They as well grow after the first layer with steps of the long molecular axis length which suggests that the molecules stack onto each other upright. The line scan illustrates this in figure 3.17 (bottom right).

The X-ray reflectivity measurements are shown in figure 3.18 for different spin speeds together with their fits. At 1600 rpm and above fringes disappear indicating a film thinning which is again in accordance to spin coating theory

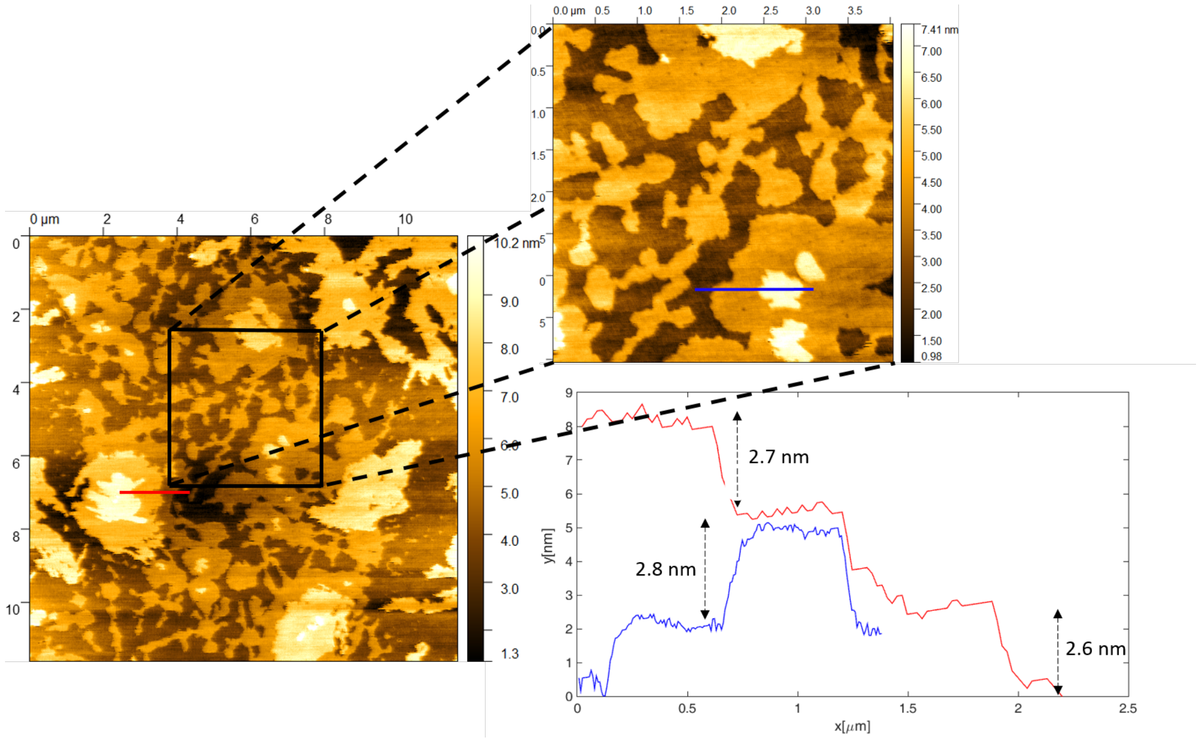

Figure 3.17: AFM measurement of a sample spin coated with a concentration of 0.7 g/l. The surface is shown in the overview picture (left) and in the magnification (upper right). Furthermore the linescans of the blue and red regions are given (bottom right) together with the step height.

that assumes greater convective radial outflow of the solution with increasing spin speeds.

The fits give similar results as for 0.5 g/l and are illustrated in figure 3.19. It still remains difficult to obtain a proper fit, although by letting the program set the third layer to zero density it succeeds. The density values and lengths of the layers in the model are illustrated in figure 3.19 by arrows with different color shading. The results indicate that the lower dense alkyl chains point towards the substrate. This suggests again that the molecules change their

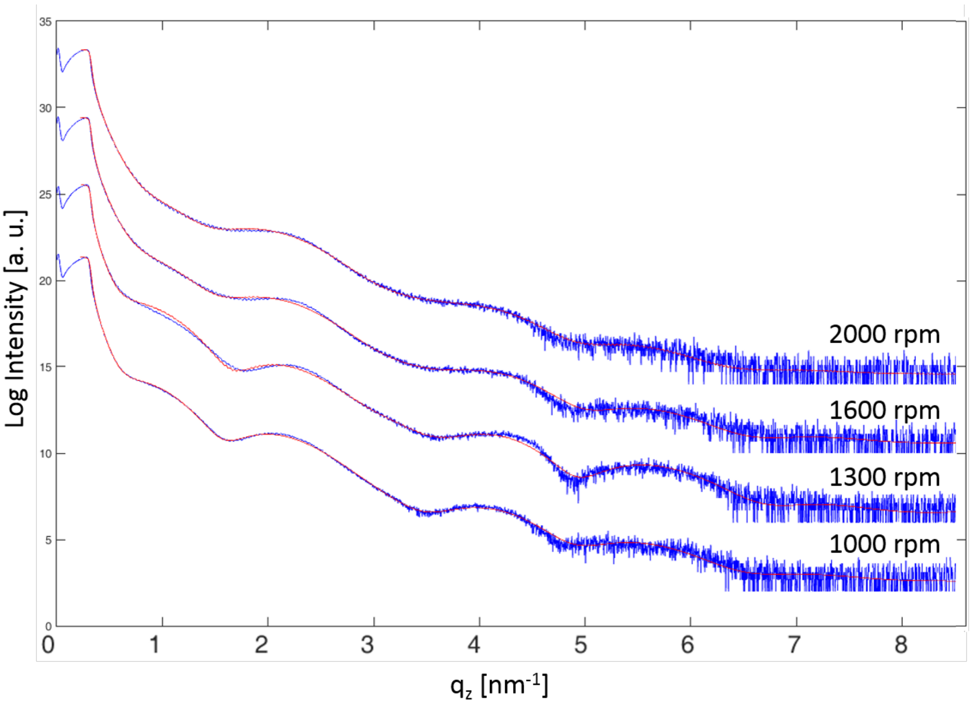

Figure 3.18: X-ray reflectivity measurements of samples spin coated with a concentration of 0.7 g/l. The curves represent different spin speeds between 1000 and 2000 rpm and are illustrated together with their fits (red).

orientation when starting to form multiple layers. The total length of all layers in the model is between 5.7 nm and 5.6 nm which is only slightly higher than two molecules stacked on each other.

	1000rmp	1300rmp	1600rmp	2000rmp
Layer 4	1,90 0,52	1,90 0,43	1,82 0,29	1,78 0,25
Layer 3	1,01 0	0,41 0	1,29 0	1,16 0,20
Layer 2	1,12 1,18	1,70 0,68	0,80 1,50	1,09 1,30
Layer 1	1,65 0,53	1,66 0,59	1,70 0,63	1,60 0,68

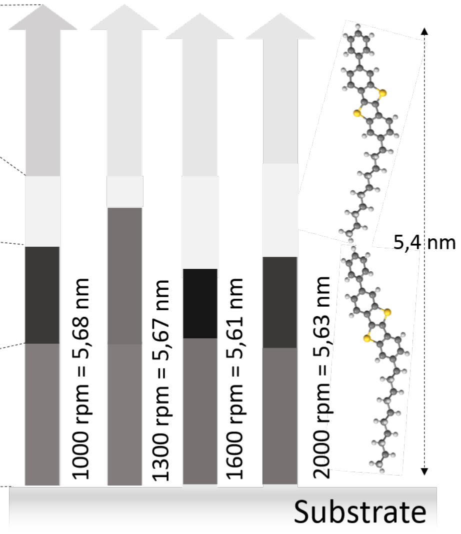

Figure 3.19: The table (left) shows the X-ray reflectivity fit parameters for the four layer model used to obtain the (red) curves in figure 3.18 at each individual spin speed. A illustration of the density distribution and total length of each model is given by respective arrows (right).

3.4 High concentrations

At a concentration of 1.2 g/l the multilayer structure observed for 0.5 g/l and 0.7 g/l remains. This is shown in figure 3.20 for spin speeds between 750 and 2000 rpm. The dashed blue lines indicate the Bragg peak positions of the bulk crystal structure calculated by the structure factor. Intensities grow at these positions. Especially the 002 peak at q = 2.37 nm^{-1} develops. The curve shape doesn't change anymore so strongly with increasing spin speed.

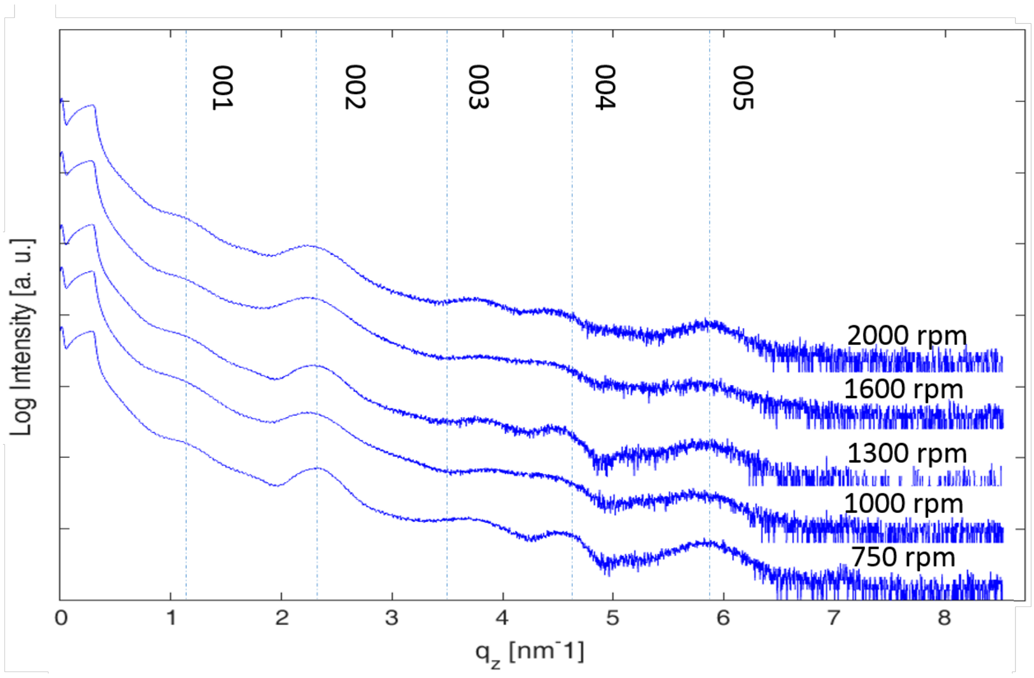

Figure 3.20: X-ray reflectivity measurements of samples spin coated with a concentration of 1.2 g/l. The different curves represent spin speeds between 750 and 2000 rpm. The vertical lines illustrate the positions of the 001 to 005 Bragg peaks of the bulk crystalline state.

The thin film morphology is visible in the optical microscope pictures illustrated in figure 3.21 . Several micrometer long islands are spread over the surface.

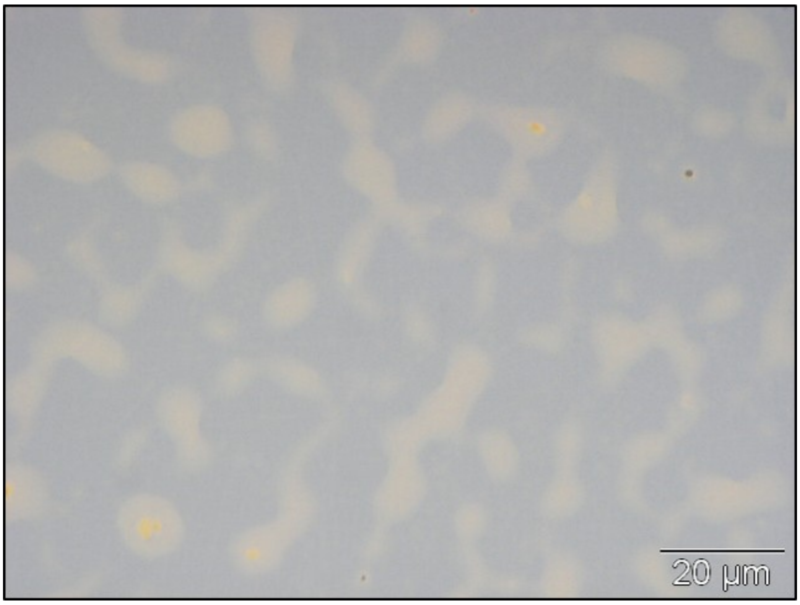

Figure 3.21: Optical light microscope picture of a sample spin coated at a concentration of 1.2 g/l at 1000 rpm. The picture was taken with a magnification of x1000.

At 1.5 g/l the features in the X-ray reflectivity curves get stronger and especially the 002 peak increases in intensity sharper as shown in figure 3.22. The microscopy pictures show that the islands increas in lateral diameter and connect to each other. A few micrometer big crystals can already be spotted as well.

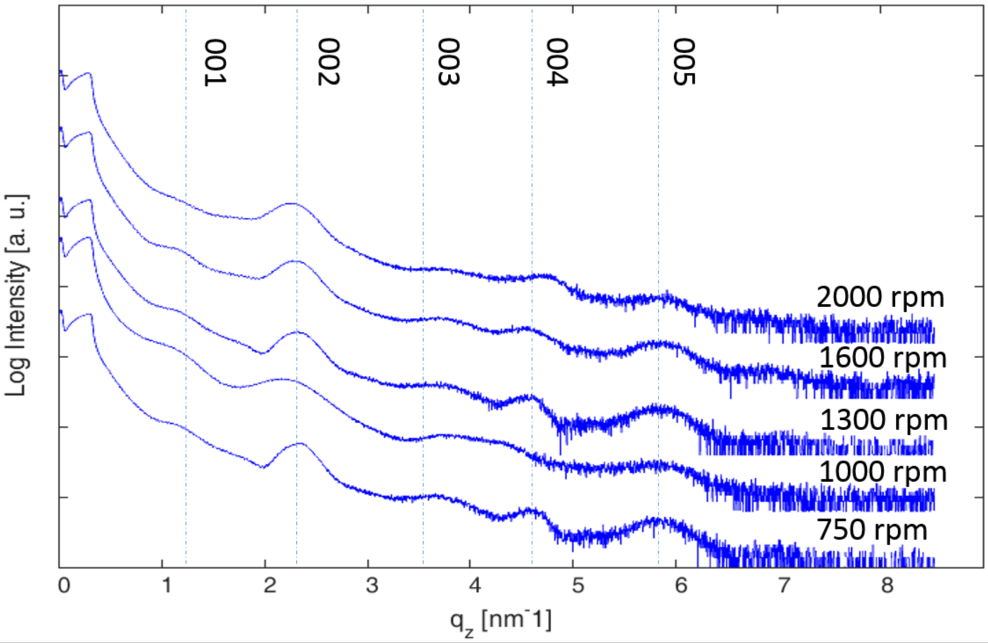

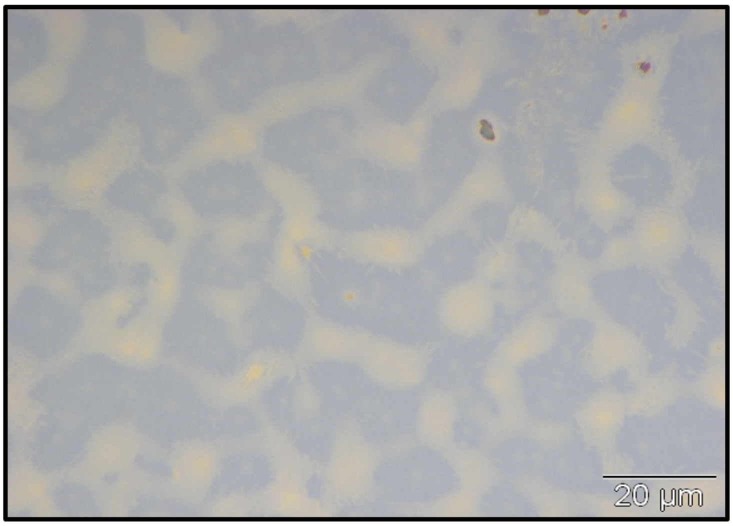

Figure 3.22: XRR curves for 1.5 g/l at different spin speeds between 750 rpm and 2000 rpm (top). An optical microscope picture of the 1600 rpm sample is shown below. (bottom)

AFM measurements like in figure 3.23 give further insight to the thin film morphology showing big rod like islands that plough through the image. The islands still grow in steps of one upstanding molecule shown in figure 3.23 (red). The dendritic structure forming the lowest layer in contact with the substrate is again smaller than the long axis molecular length (blue).

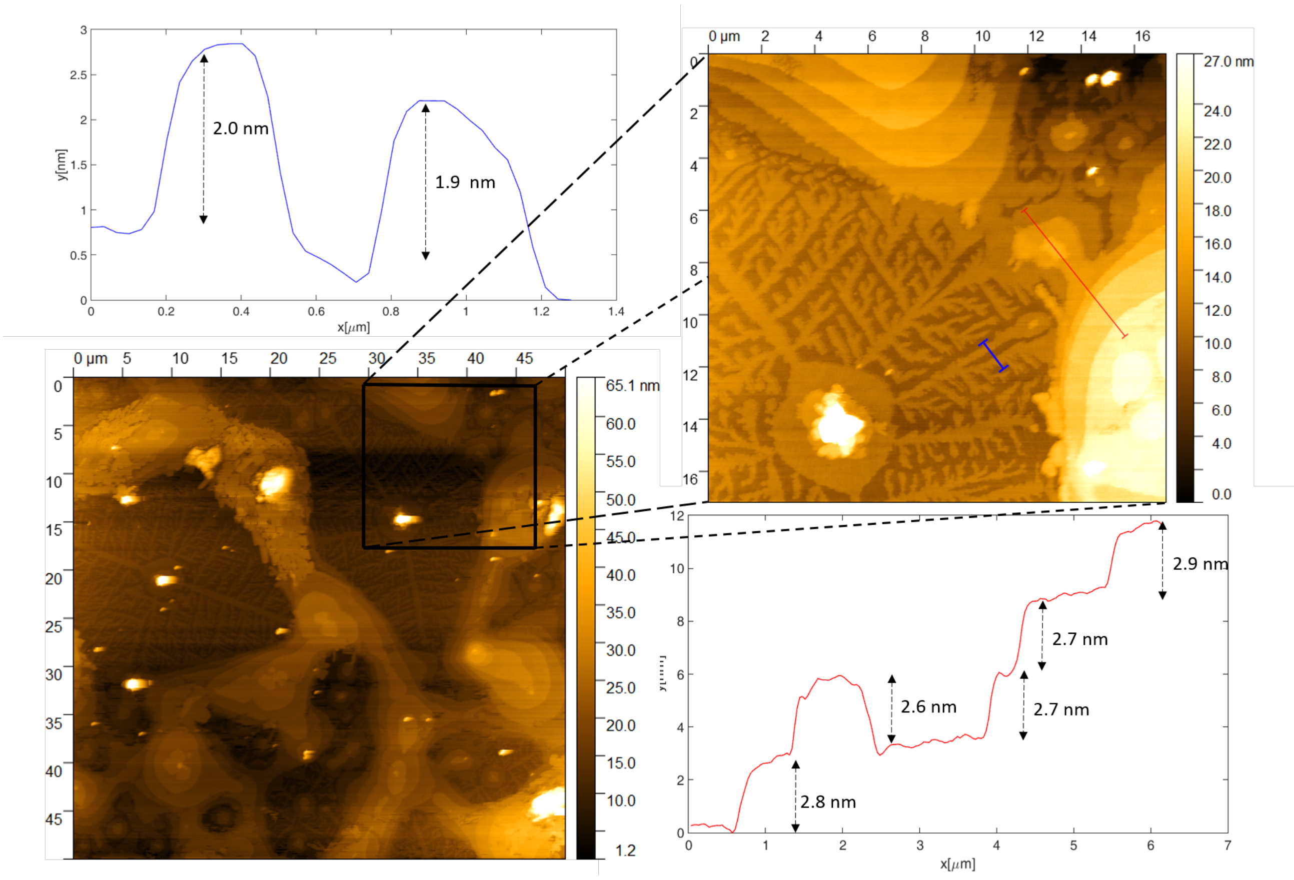

Figure 3.23: AFM measurement of a sample spin coated at a concentration of 1.5 g/l. An overview picture (lower left) and a magnification (upper right) is shown. The height profile of the marked regions (blue and red) is given as well (upper left and bottom right).

This reinforces the discussion from above suggesting a specific cantilever-surface interaction when passing from the stiff substrate to the softer organic film that reduces the measured layer height.

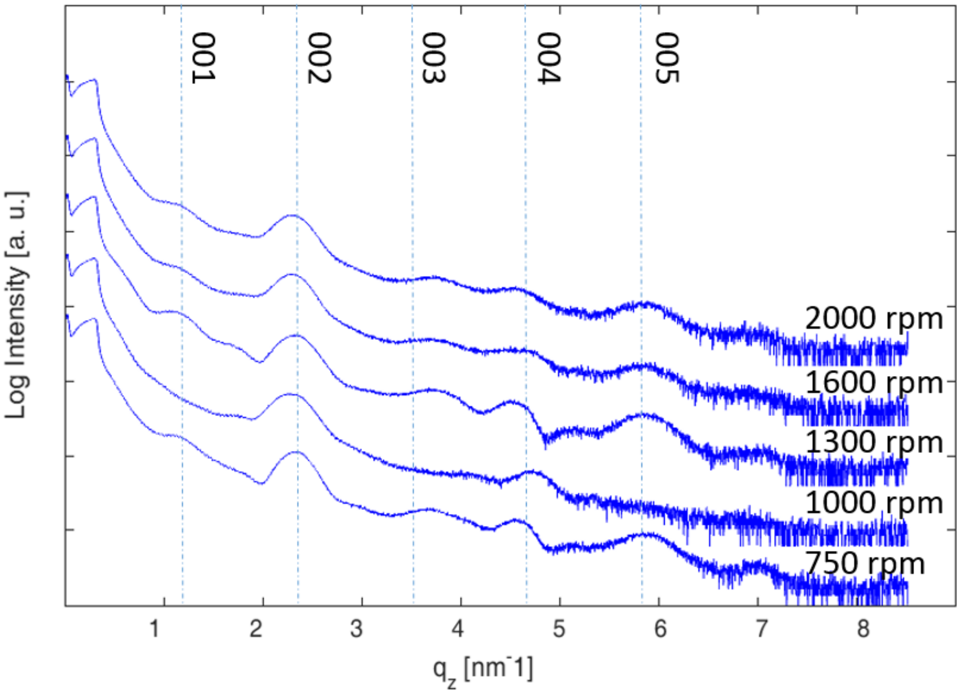

Figure 3.24: X-ray reflectivity measurements of samples spin coated with a concentration of 2 g/l. The different curves represent spin speeds between 750 and 2000 rpm. The vertical lines illustrate the positions of the 001 to 005 Bragg peaks of the bulk crystal phase.

Nearly the same tendency is observed for another concentration increase to 2 g/l. From figure 3.25 it is apparent that crystals start to grow that are of several micrometer in diameter and clearly visible. It seems that the intensity of the Bragg peaks is mainly driven by the amount and size of crystallites present. In figure 3.24 the peaks get even bigger except for 1000 rpm were every second peak disappears which indicates a crystal E like structure as will be discussed further ahead.

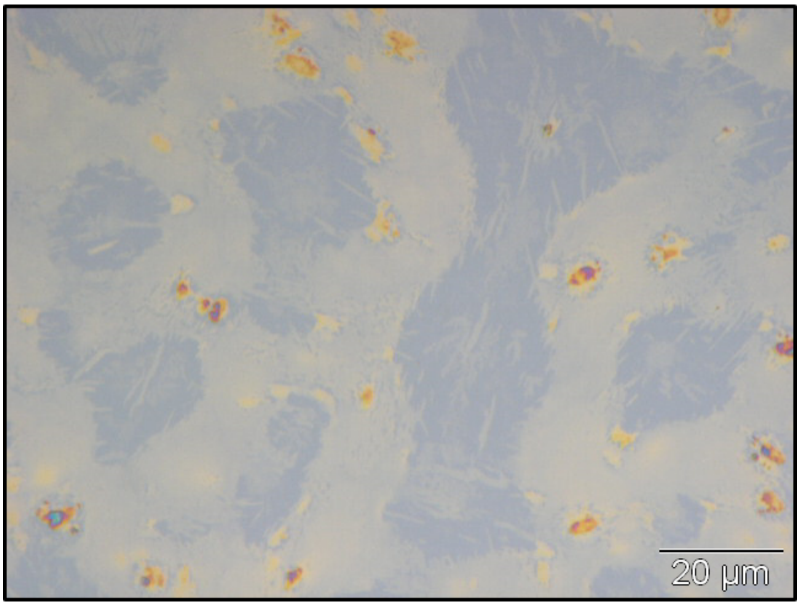

Figure 3.25: A optical light microscope picture of a sample spin coated with a concentration of 2 g/l at 1000rpm. It was shot with a magnification of x1000 and shows many crystals spread over a partly covered surface.

At a concentration of 3 g/l more crystallites appear as shown in the light microscopy pictures in figure 3.26. The peaks get slightly stronger than for 2 g/l. The reflectivity curves for different spin speeds don't exhibit a significant change, although for 1300 rpm the peaks are sharpest.

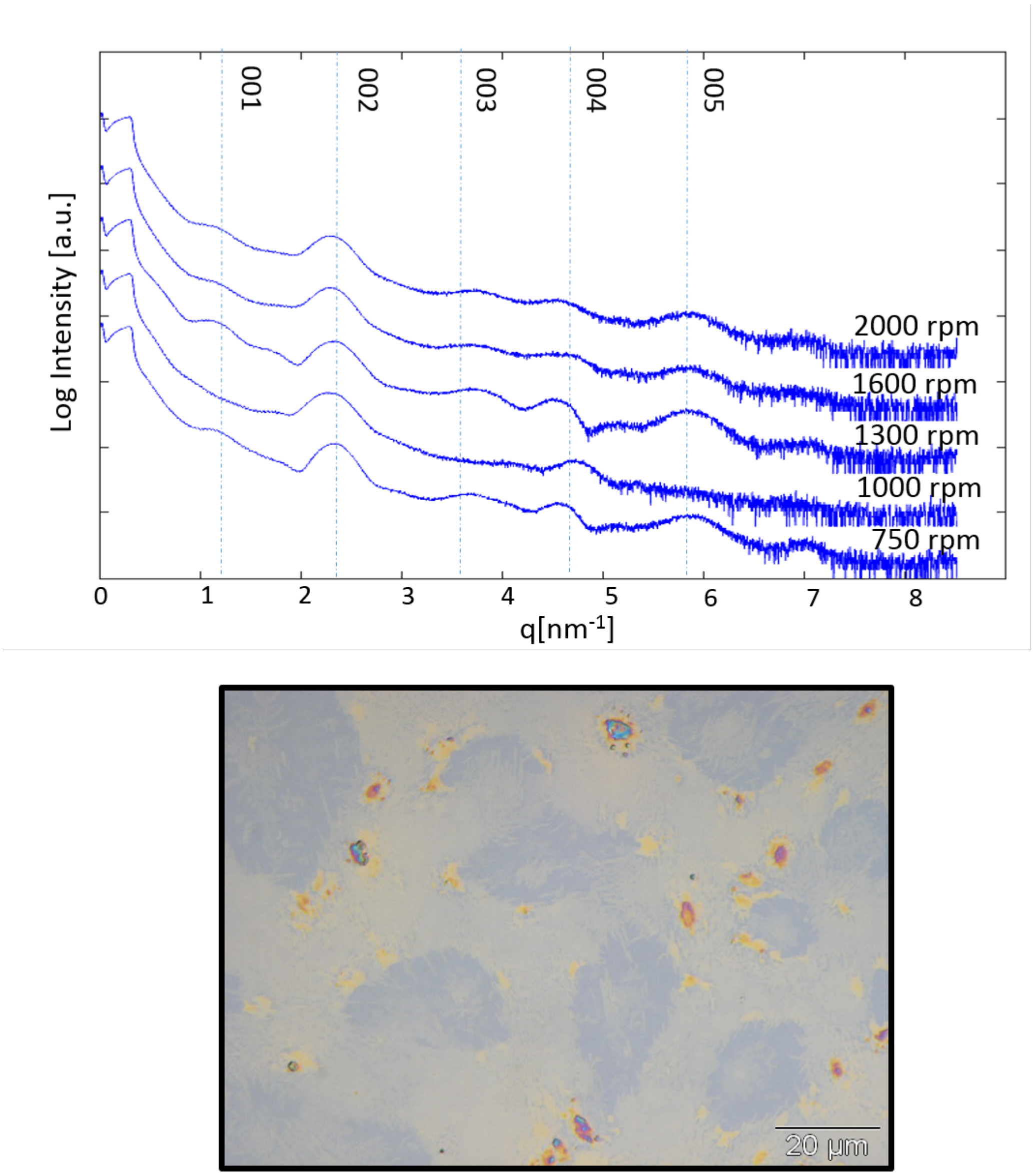

Figure 3.26: XRR curves for 3 g/l at different spin speeds between 750 and 2000rpm (Top). An optical microscope picture of the 1300 rpm sample is shown below. (bottom)

At 5 g/l the bulk crystal structure clearly dominates the pattern of the X-ray reflectivity measurements as illustrated for increasing spin speeds in figure 3.27. Except for 1300 rpm all measurements have sharp bulk Bragg peaks.

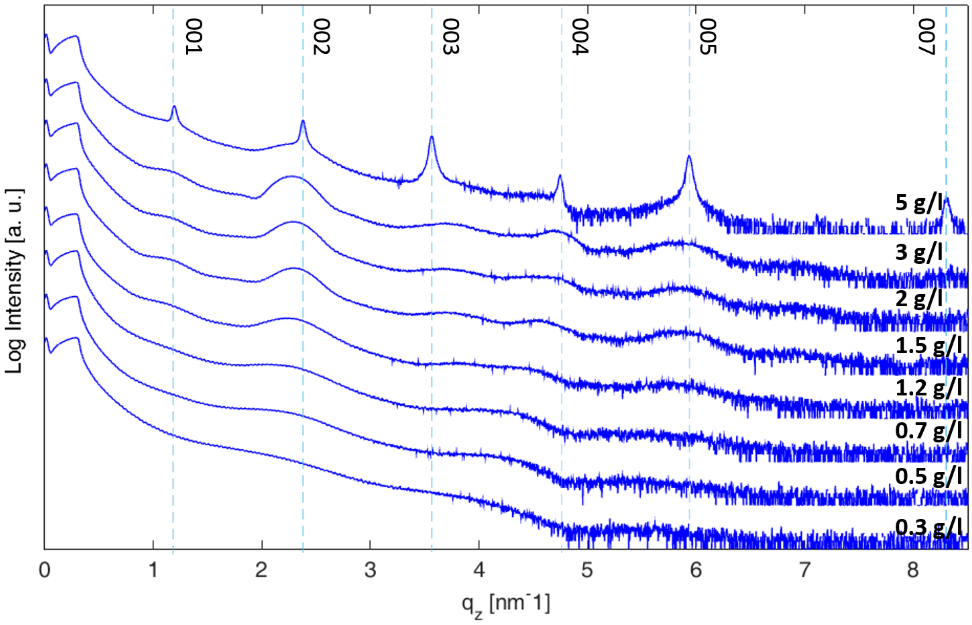

Figure 3.27: X-ray reflectivity measurements of samples spin coated at a spin speed of 1600 rpm. The concentration varies between 0.3 and 5 g/l.

Figure 3.28 shows the X-ray reflectivity measurements for different spin speeds (top) and a optical microscope picture (bottom). Big crystallites with diameters around 20 μm are formed together with small ones of a few micrometers. They grow out of a fully covered background surface. The XRR curves show Bragg peaks at positions corresponding to the bulk crystalline phase.

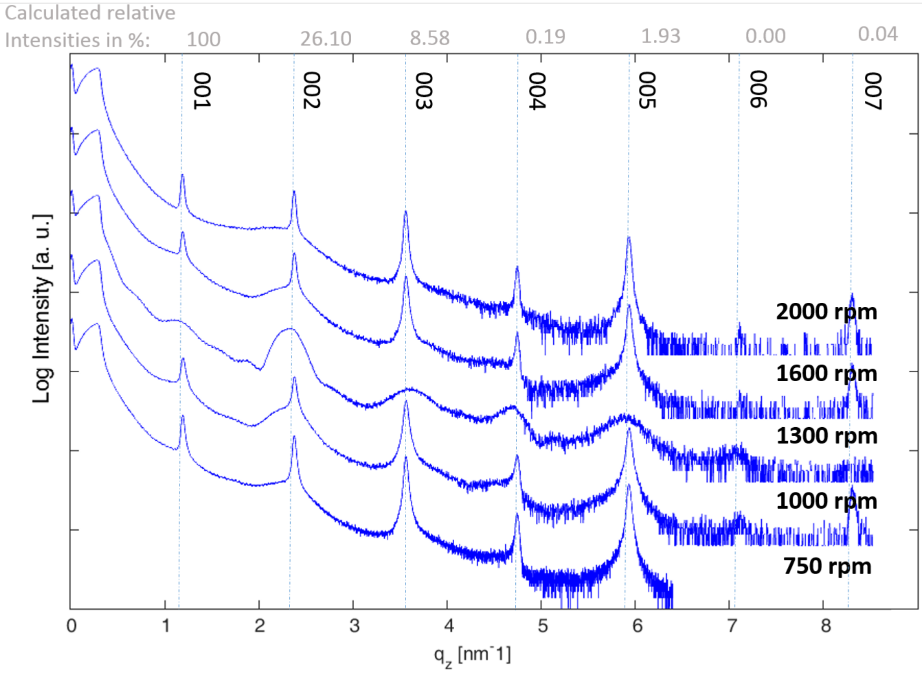

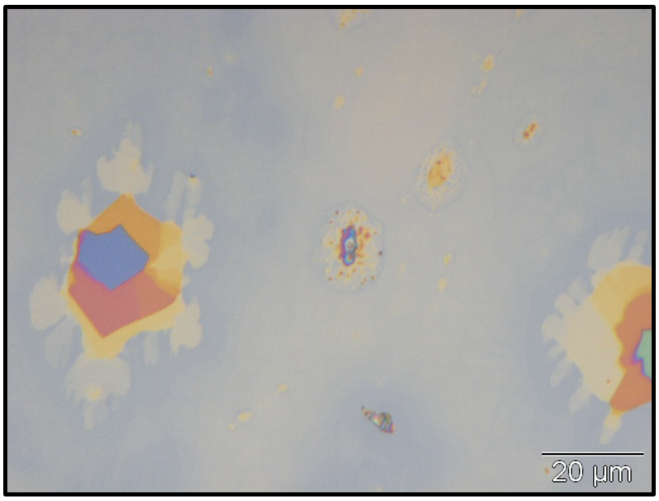

Figure 3.28: X-ray reflectivity measurements of samples spin coated at a concentration of 5 g/l and spin speeds between 750rpm and 2000rpm. (top) A optical light microscope picture showing the surface structure (bottom).

To investigate the Bragg peaks of the crystal structure at higher orders a specular X-ray diffraction measurement was performed. The scan range was set between 5° and 32° and the resulting figure was overlapped with a reflectivity measurement between 0° to 11°. Figure 3.29 shows the plot with the blue line representing the XRR data and the red line the specular XRD data. The calculated relative intensities of the bulk phase are given (gray) and are more or less in accordance with the measurement.

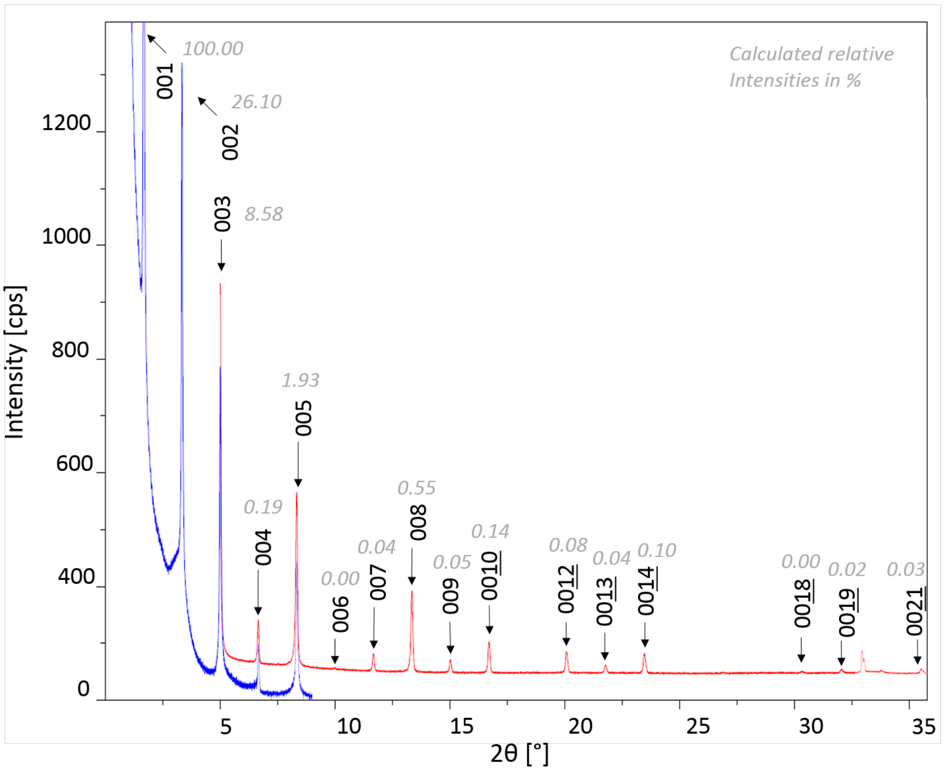

Figure 3.29: Bragg peaks of a sample spin coated with a concentration of 5 g/l. An X-ray reflectivity measurement (blue) and a specular X-ray diffraction measurement (red) are overlapped showing the full range between 0° and 37°.

The first peak is at 1.66° which corresponds to a inter planar distance of 5.3 nm derived from Bragg's law.

$$d = \frac{0.154nm}{2 * \sin(1.66^\circ/2)}$$

All following peaks are at a multiple of the 001 peak. The peak positions are in accordance with the bulk Ph-BTBT-10 crystal structure observed in former powder diffraction studies.[19] The unit cell is illustrated in figure 3.30 (left) and shows two molecules head to head and slightly tilted towards each other. The space filling model is shown to the right.

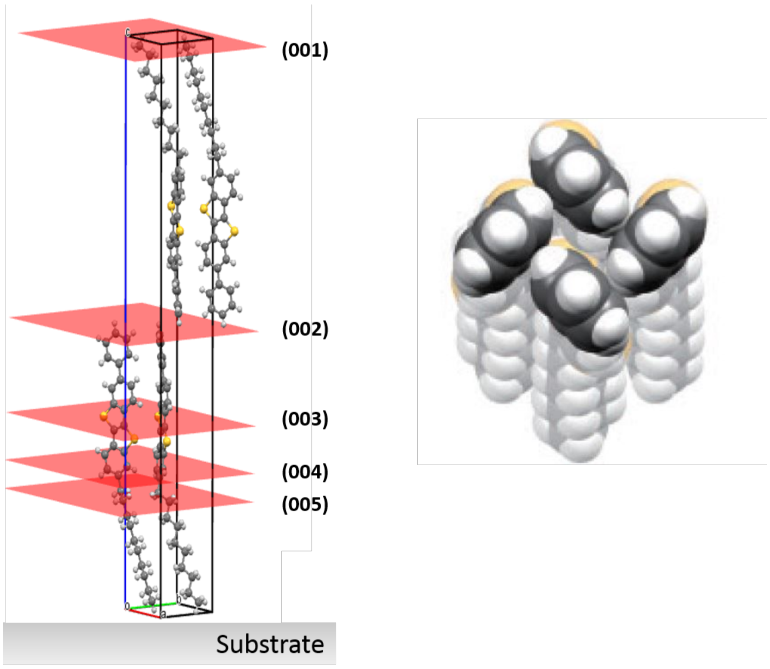

Figure 3.30: The unit cell of the bulk crystal structure with the 001 plane and its multiplies marked in red. (left). The herringbone packing viewed from above in the space filling model.(right)[19]

Because only the 001 plane and its multiplies are observed it can be concluded that the crystal structure grows with the long axis perpendicular to the substrate surface. The bulk phase has a herringbone structure as shown in figure 3.30 (right) and the unit cell is orthorhombic with a long axis length of c = 5.3124 nm, a width of a = 0.60471 nm and a depth of b = 0.77568 nm.

To also clarify the in-plane structure GIXD measurements where performed. Figure 3.31 shows the measurement in which q_{xy} is plotted vs. q_z. The rod of intensity points at q_{xy} = -1.32 (blue arrow) appears due to the 11L planes. The circles represent the expected intensity values of each peak calculated by the structure factor. They are in good accordance with the measurement. An illustration of the most intense 112 and 115 planes is given in figure 3.32 (left) inside the unit cell and in figure 3.32 (right) in the packing structure. At the right bottom corner of figure 3.31 q_{xy} equals zero which means the q vector stands perpendicular towards the surface and resembles a reflectivity measurement. The high intensity points (white arrow) correspond to the 003, 004, 005 Bragg peaks. The 001 and 002 peaks are absorbed by the beamstop which protects the detector from getting overshot. In the left bottom part of the measurement at q_{xy} = -1.93 (red arrow) the intensity points corresponding to the 12L are visible too.

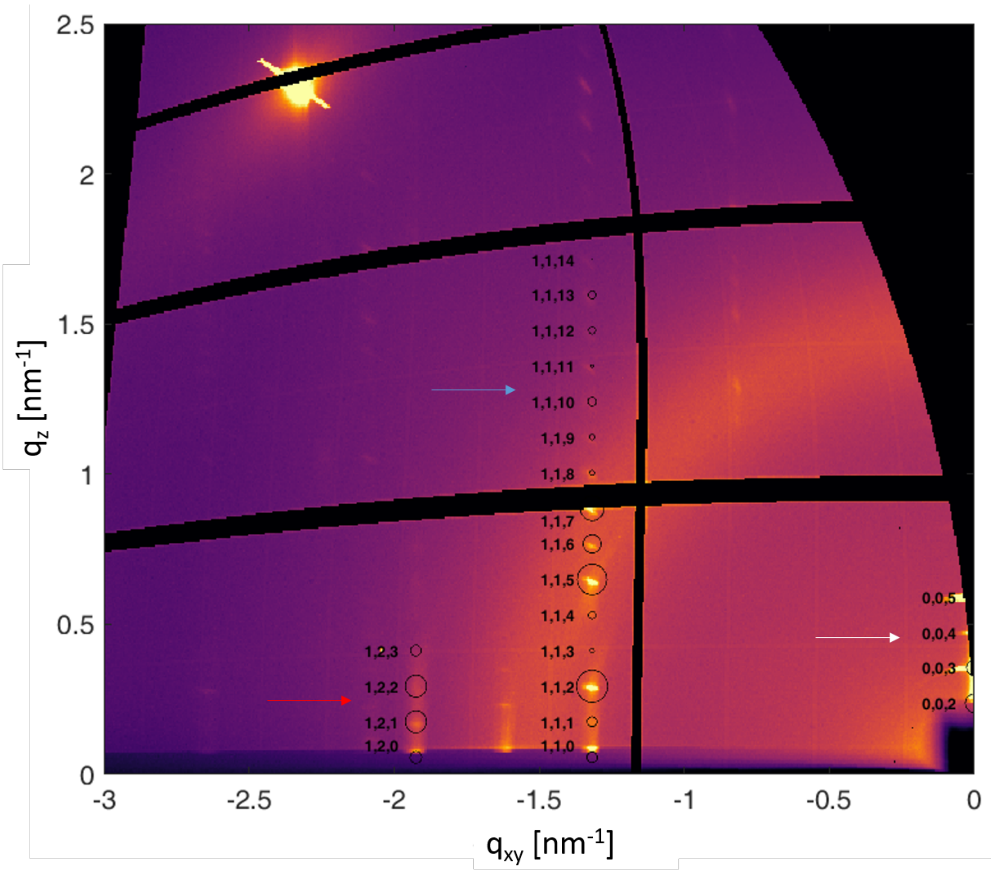

Figure 3.31: Grazing incidence X-ray diffraction measurement of a bulk crystal sample. The radii of the circles surrounding each intensity point represent the expected intensity values calculated by the structure factor.

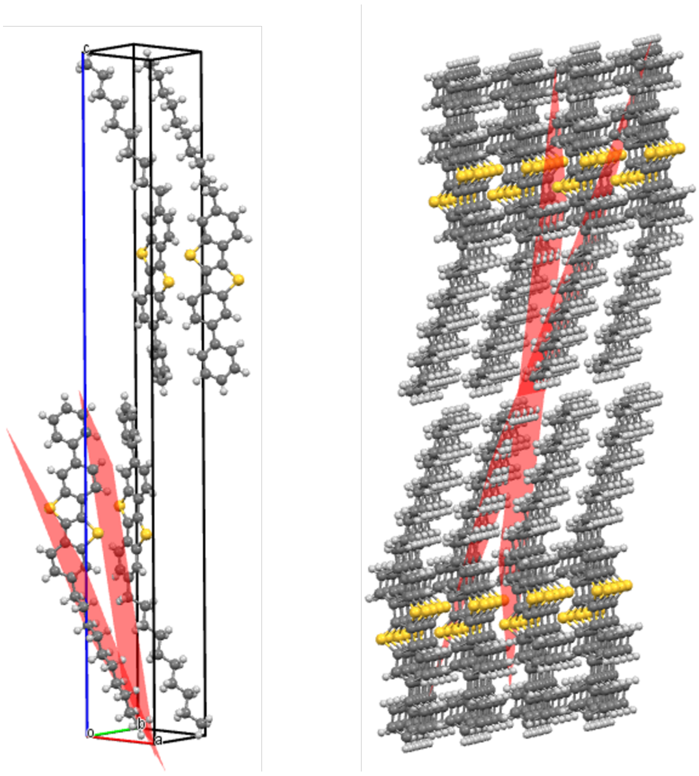

Figure 3.32: Illustration of the bulk crystal structure unit cell with the 011 and 012 plane marked in red. (left). The planes are also shown in the stacking simulation. (right)

Besides the bulk crystal structure another phase is observed while spin coating. It appears at concentrations between 1.5 g/l and 5 g/l and is shown in figure 3.33 together with the respective spin speeds. Compared to the bulk phase only every second peak remains. This is most clearly visible for the violet curve at 1600 rpm and 5 g/l. Such a structure is present in the crystal E phase of Ph-BTBT-10 which will be discussed ahead, the peaks are too broad though to be classified as such.

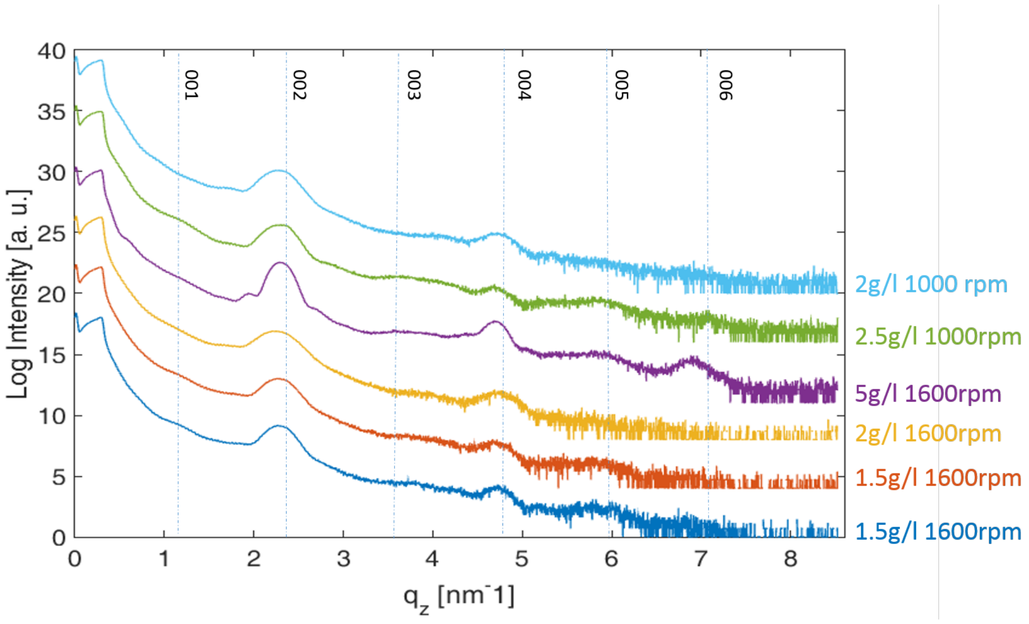

Figure 3.33: The X-ray reflectivity curves of samples that show the disordered crystal E phase together with their respective concentrations and spin speeds.

According to the Scherrer equation the peak width of the violet curve in figure 3.33 corresponds to a crystallite size of 26 nm.

$$L = \frac{0.15405nm}{0.00576 * \cos(3.22°)}$$

The prevalent phase appears to be a kind of disordered crystal E phase containing a certain degree of disorder in out-of-plane direction. Figure 3.34 gives a schematic illustration of the assumes arrangement. Figure 3.35 shows an optical microscope picture of the sample corresponding to the violet curve in figure 3.33. The background is fully covered and small islands are visible.

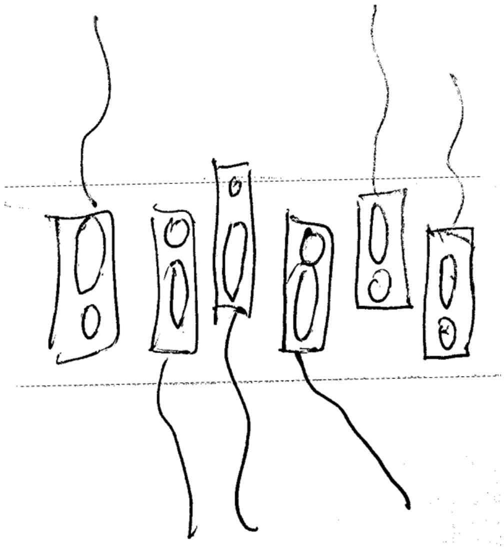

Figure 3.34: Illustration of the assumed packing behaviour of the molecules in the disordered crystal E phase.

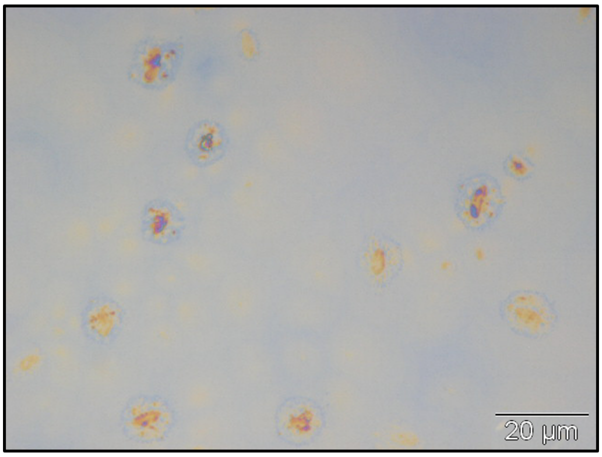

Figure 3.35: Optical light microscope picture of the sample showing the violet reflectivity curve in figure 3.33 possessing the disordered Crystal E phase.

3.5 Heat Treatment and Phase Transitions

Previous calorimetric studies on Ph-BTBT-10 revealed that there are three different phases present between room temperature and the melting point.[10] Figure 3.36 shows the observations with the red line representing the heating cycle and the blue line the cooling cycle. The bulk crystal phase remains stable during heating until around 143°C after which it goes over into the crystal E phase (smectic E). There it remains stable until 210°C before changing to the smectic A phase. At around 223°C the melting point is reached. During cooling the liquid to smectic A and the smectic A to crystal E transition temperatures remains at 223°C and 143°C respectively. The temperature for the transition from crystal E to bulk crystalline is shifted though, to around 99°C .

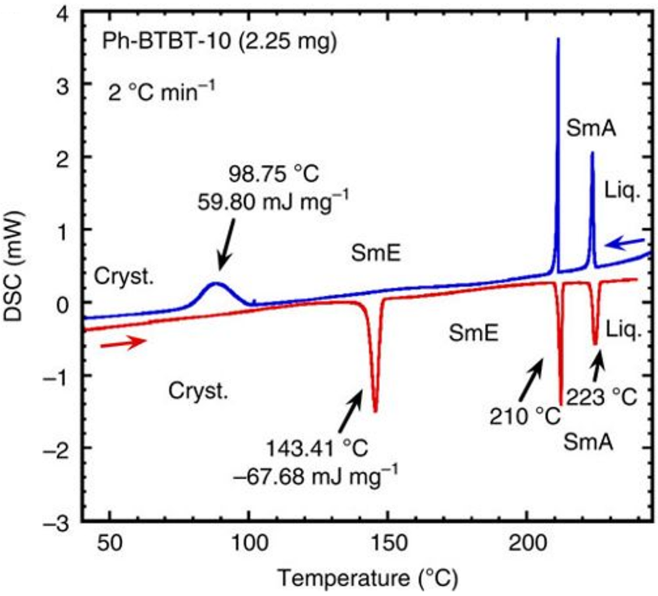

Figure 3.36: Differential scanning calorimetry measurement of Ph-BTBT-10 showing the heating and the cooling cycle with its respective phase transition temperatures.[10]

In this work in-situ temperature studies were performed using a DHS 900 to precisely observe the transition behavior and its points of occurrence. The measurements were done using the PEEK dome which was filled with nitrogen gas to create the protective atmosphere against oxidation. The sample was heated with heating rates between 0.14°C and 0.16°C per minute close to the transition points and with 5°C to 10°C per minute further away. To understand the transition behaviour as good as possible X-ray reflectivity measurements were performed in two different angular ranges. Over a long range between 0° and 11° to examine the behaviour of the Bragg peaks corresponding to the 001 002 003 004 and 005 planes of the bulk crystal structure. And over a shorter angular range between 2.25° and 6° to particularly focus on the two Bragg peaks of the 002 and 003 plane. For the investigation of the phase transitions described in the DSC measurements above, samples with the highest concentration of 5 g/l where used that showed a strong bulk signal with clear peaks. From 25°C up to 145°C no significant change of the signal is observed. The transition from bulk crystalline to the crystal E structure appears at around 149°C as shown in figure 3.37. During this transition the bulk 002 peak at 3.3° diminishes and gives rise to a new peak at 3.1°. Moreover the 003 peak at 4.9° vanishes completely.

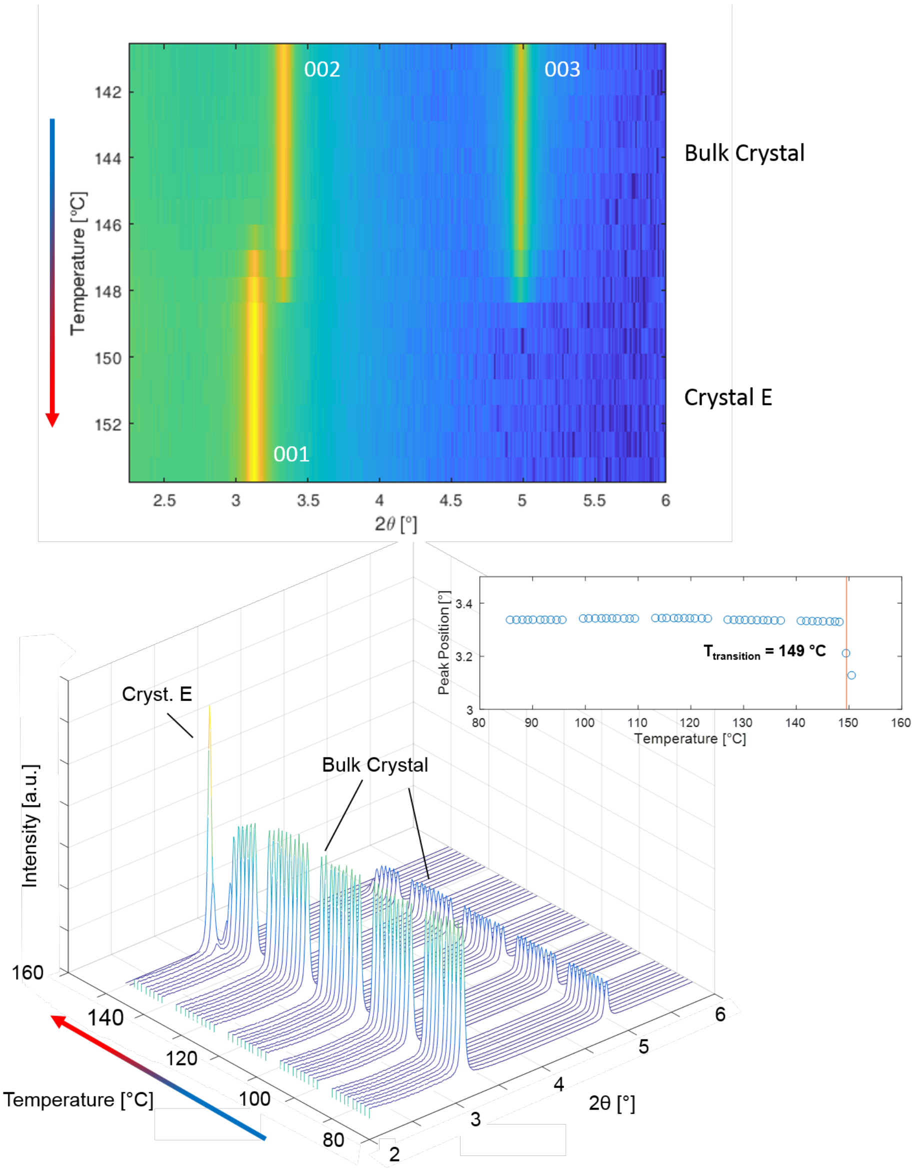

Figure 3.37: X-ray reflectivity measurements between 2.25° and 6° performed during heating from 85°C to 155°C (bottom) and shown in more detail with a surface plot between 140°C and 155°C (top). The Phase transition from bulk crystalline to crystal E is visible at around 149°C.

A long range scan at 155°C is shown in Figure 3.38 (red) and is compared to the bulk crystalline structure at room temperature (blue). The comparison reveals that the 001 and 005 peak diminish as well while the 004 peak at q = 4.74 nm^{-1} shifts to q = 4.42 nm^{-1}. Overall every second peak vanishes and the remaining peaks are shifted to lower degrees. The new 001 peak is at q = 2.2 nm^{-1} and the new 002 peak at q = 4.42 nm^{-1}. This corresponds to a interplanar distanc of 2.7 nm as calculated by Bragg's law.

$$d = 0.154nm/(2 * sin(3.3°/2))$$

This is comparable to the length of one standing molecule and in accordance with a crystal E structure studies.

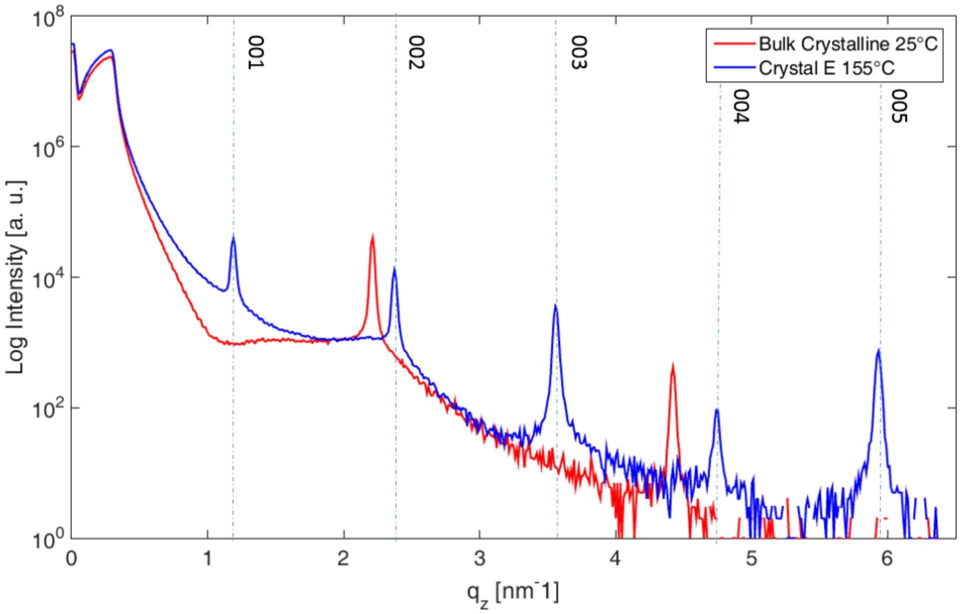

Figure 3.38: X-ray reflectivity measurement of a bulk crystal sample at 25°C (blue) compared to its crystal E phase (red) at 155°C.

How the molecules rearrange during the phase transition exactly and which position they finally take towards each other in the crystal E phase is still not fully understood. There are however two common packing models for the crystal E phase. The traditional crystal E structure and a nano segregated structure. Figure 3.39 illustrates the transition from the bulk crystal phase (left) with its head to head arrangement to the crystal E phase with the two different packing models (right).

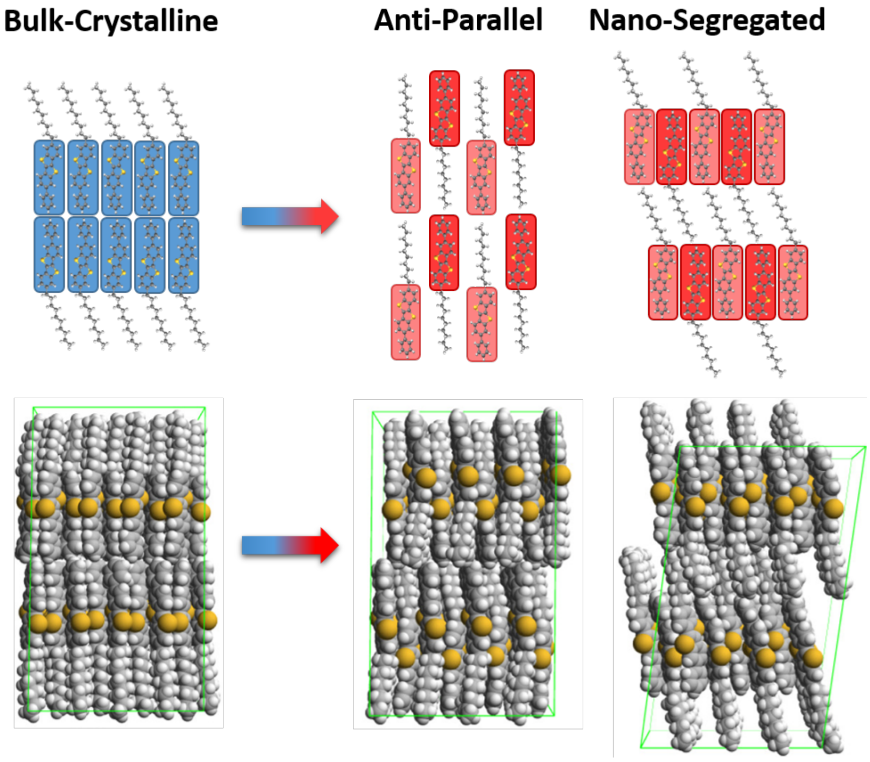

Figure 3.39: The bulk crystal structure with its head to head arrangement (left) and the crystal E structure with its two different packing models (right). The anti-parallel packing model with a alternating head to tail arrangement (I.) and the nano-segregated packing model with alternating core and alkyl chain layers (II.).[34]

The traditional crystal E structure was proposed in 1991 and assumes that the packing depends strongly on the shape of the mesogenic molecules whether they are symmetric with two flexible alkyl chains on both ends, or asymmetric with only one alkyl chain like for Ph-BTBT-10. For the asymmetric case the molecules are supposed to take an anti-parallel arrangement towards each other as shown in figure 3.39 (I.). Diele notes in his studies that the unit cell slightly grows with the antiparallel arrangement and therefore observes a small peak shift to smaller degrees in the X-ray diffraction measurements just as for our studies.[5] The second packing model of the crystal E structure, the so called nano-segregated structure was recently discovered in 2013. It is shown in figure 3.39 (II.) and assumes a laminar segregation of the aromatic cores by their alkyl chains. The arrangement leads to a triclinic unit cell that in some cases might allow the alkyl chains to freely move within their plane. [21] Which of both arrangements the molecules take in our studies is still an open question and has to be analyzed further by in-plane GIXD studies.

This phase transition from bulk crystalline to the crystal E structure is reversible. By slowly cooling down the sample it completely transforms back into the bulk crystalline state. The phase transition is shown in figure 3.40. Similar to the calorimetric measurements shown above in figure 3.36 the temperature of occurrence is at around 103°C. The 001 crystal E peak at 3.1° diminishes and gives rise again to the 002 peak of the bulk structure at 3.3°. The 003 peak of the bulk structure reappears at 4.9°. The peaks loose intensity though which indicates that crystallinity is lost.

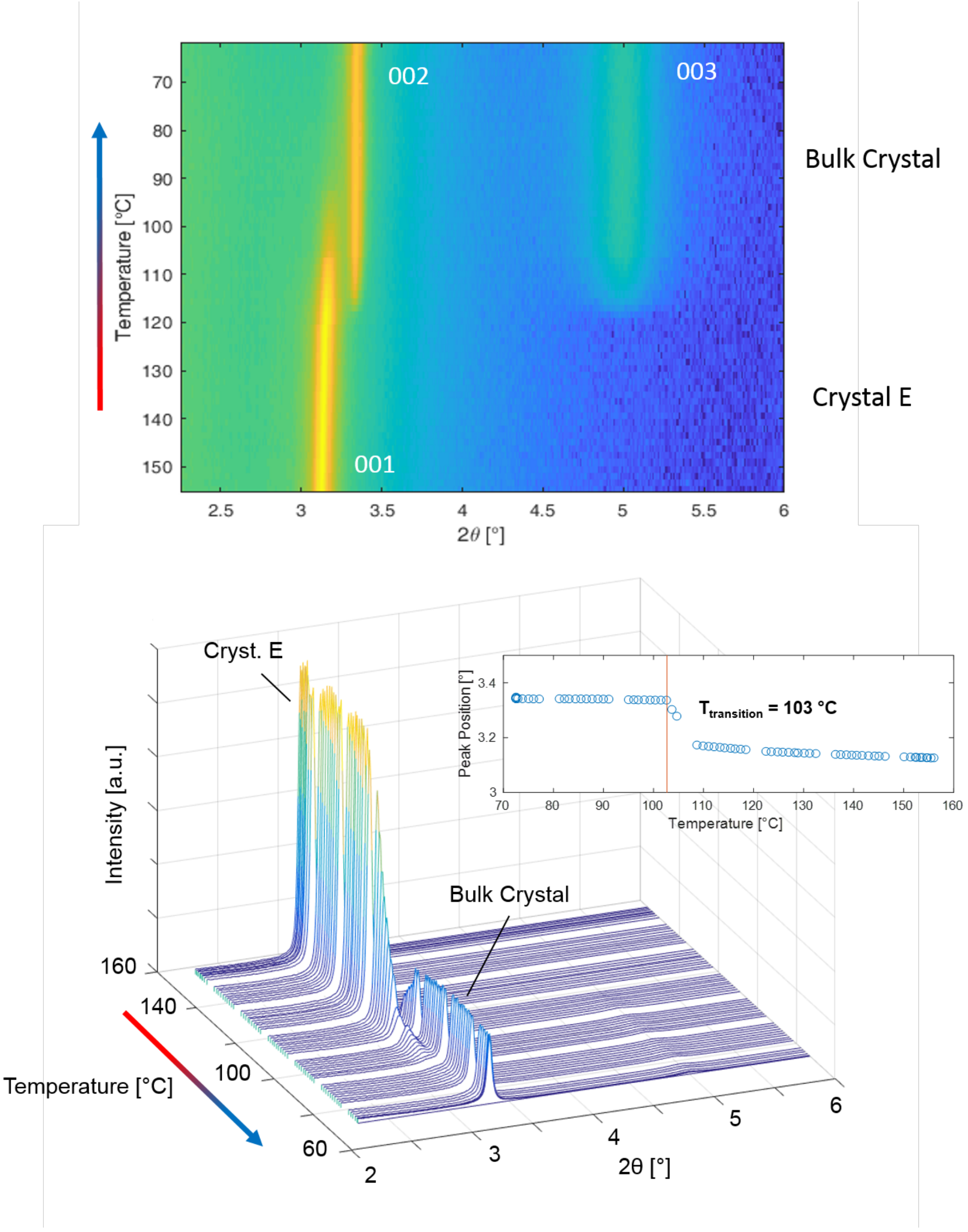

Figure 3.40: X-ray reflectivity measurements between 2.25° and 6° performed while cooling from 155°C to 70°C (bottom) are illustrated in a surface plot (top). The Phase transition from crystal E back to bulk crystalline is visible around 103°C.

The crystal E phase above 149°C can be quenched down to room temperature at cooling rate over 20°C per minute. It's structure is more or less maintained into room temperature as illustrated in figure 3.41. It is assumable that with increasing cooling rates the quenched crystal E structure might maintain itself better or completely.

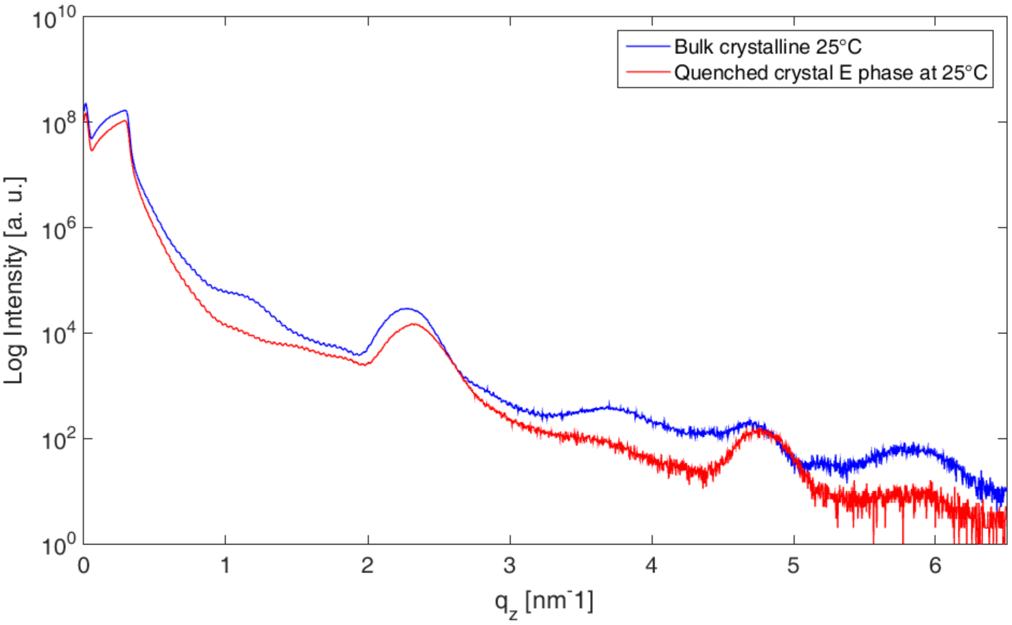

Figure 3.41: X-ray reflectivity measurement of a sample at room temperature before heating (blue) and after heat treatment, quenched from 155°C down to room temperature.(red)

When afterwards heating up the sample again the bulk crystalline structure starts to return at around 100°C as shown in figure 3.42. The Bragg peaks corresponding to the 001 003 and 005 plane return and the 002 peak shifts slightly towards a higher angle. This is in accordance with a other study in 2015 that extended the calorimetric measurement given above in figure 3.36 by preparing samples directly into the crystal E phase and afterwards temperature treating them. [10] The corresponding DSC curve is shown in figure 3.42 (upper right).

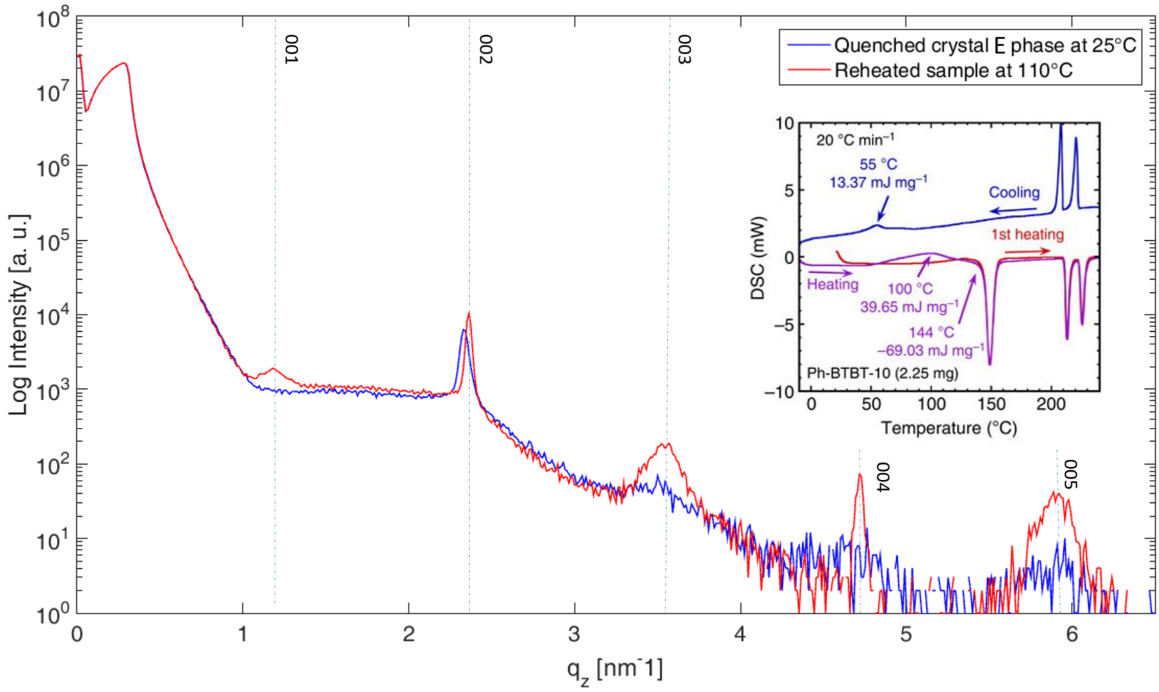

Figure 3.42: X-ray reflectivity measurement of quenched crystal E phase (blue) at room temperature and after heating up to 110°C.(red)

A very striking observation for all heated and cooled samples is the maintenance of their width during the phase transformation. Narrow bulk peaks become narrow crystal E peaks as shown above and broad peaks also maintain their shape as shown in figure 3.43 and 3.44. This behaviour appears reasonable when considering that the temperatures are far below the melting point of Ph-BTBT-10. It might be that there is sufficient energy to provoke reorientation into the new phase but insufficient to induce macroscopic structural changes. This also suggests that the bulk to crystal E transition and back doesn't go in hand with a drastic structural change but more with local reorientational movements.

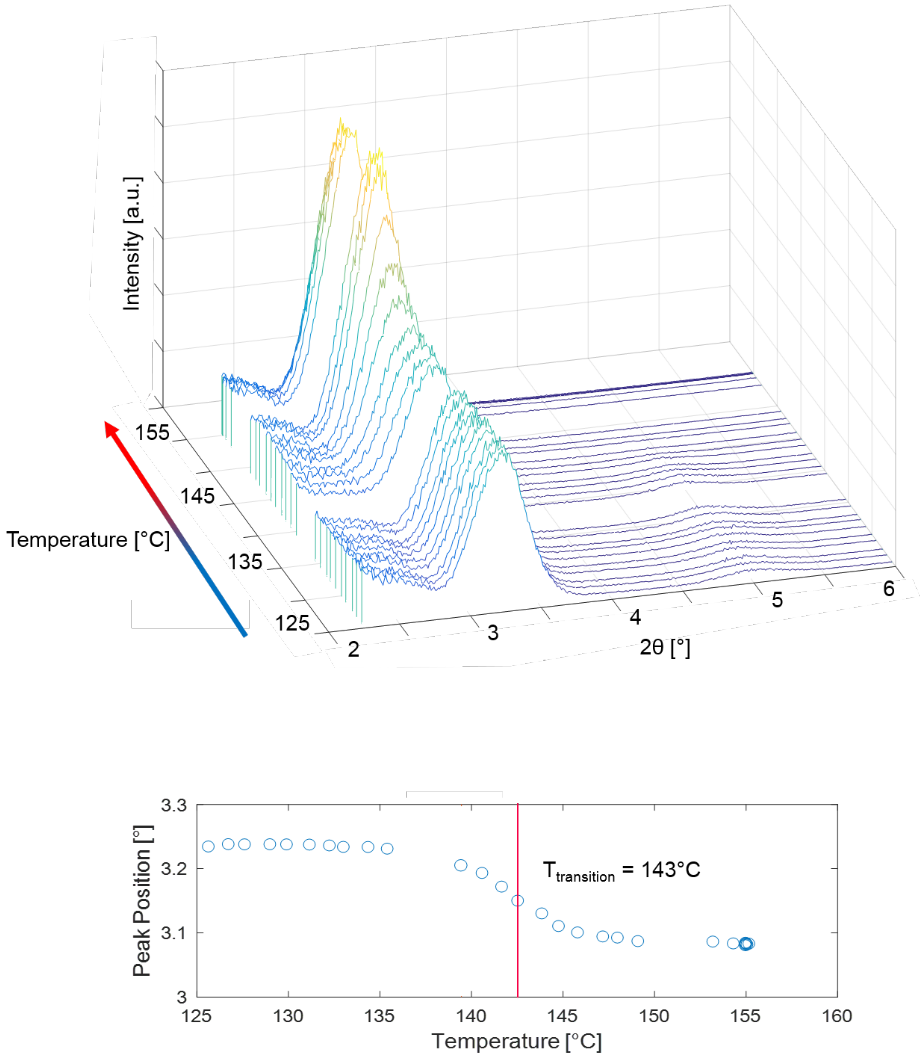

Figure 3.43: X-ray reflectivity measurement between 2.25° and 6° of a sample showing broad peaks. The width doesn't change significantly.

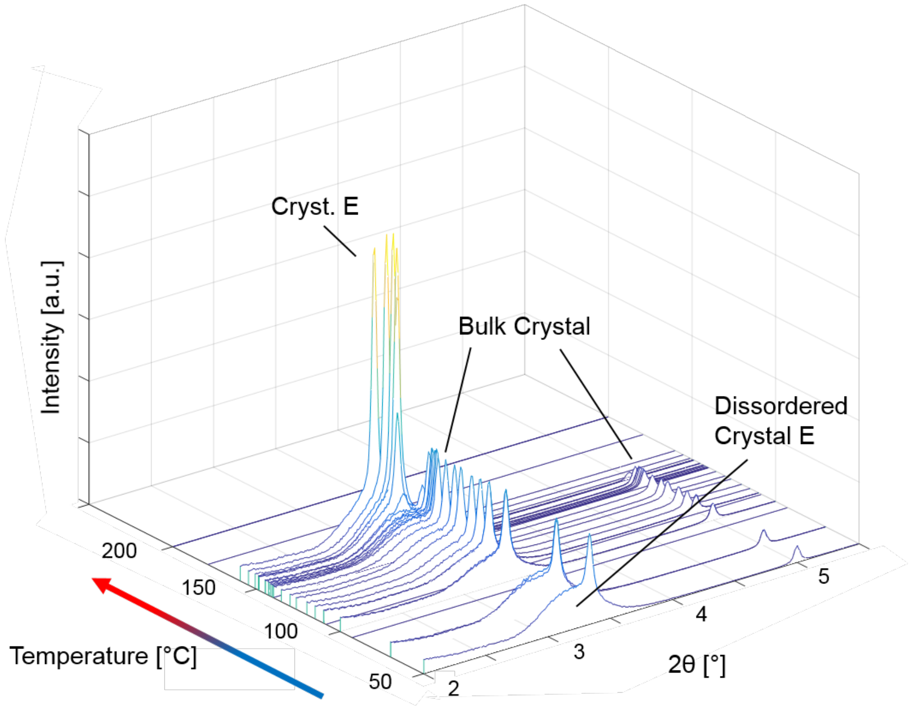

Figure 3.44: X-ray reflectivity measurement between 2.25° and 6° of a sample showing sharp peaks with a broad background. The widths of both peaks are maintained and the background peak doesn’t gain intensity.

The samples that obtain a disordered crystal E phase after spin coating described above in figure 3.33 show a similar behaviour during heating like the quenched crystal E phase illustrated in figure 3.42. The peaks of the bulk phase start to grow around 100°C and disappears again at around 149°C. The peaks maintain their width: 0.33° FWHM before and 0.31° FWHM after phase transition. They slightly move towards smaller angles as shown in figure 3.45. The figure also demonstrates an overlap of the disordered crystal E phase at room temperature, at 130°C and at 150°C after the crystal E transition. The structure is very similar which thereby confirms the presumption that the samples are in a disordered crystal E phase directly after spin coating at room temperature.

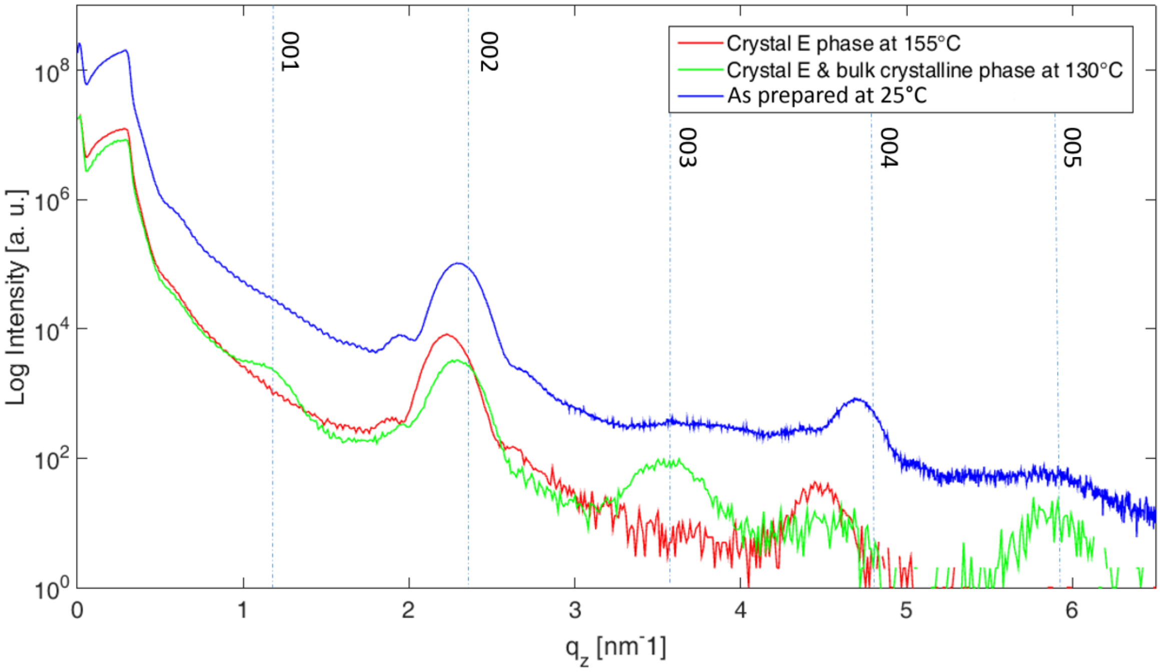

Figure 3.45: X-ray reflectivity measurements at different temperatures of the violet sample in figure 3.33 possessing a disordered crystal E phase.

The calorimetric measurement shown in figure 3.36 describes a smectic A transition at 210°C followed by the melting point at 223°C. In our study however the DHS measurements indicate that the crystal E structure stays stable until 210°C after which a sudden drop of intensity occurs as illustrated in figure 3.46.

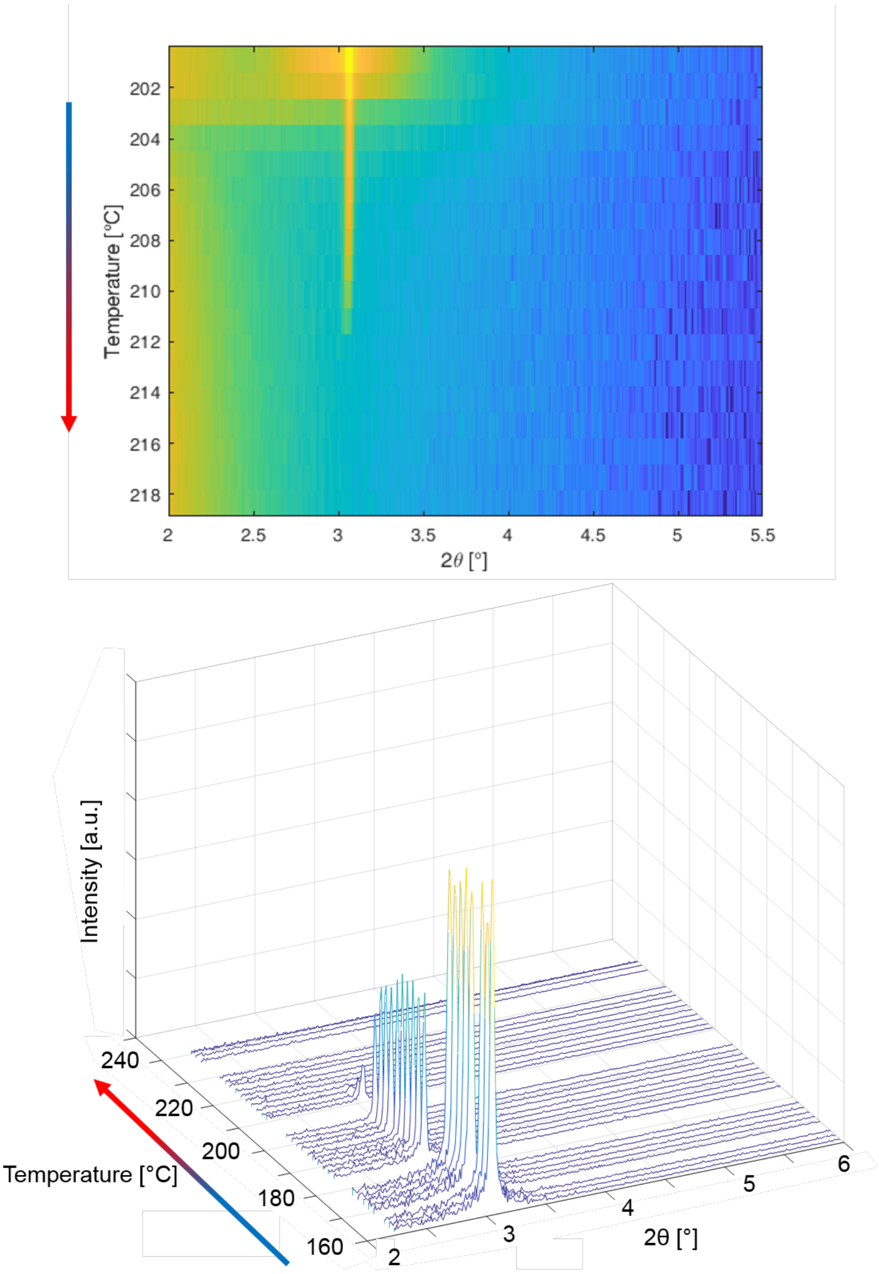

Figure 3.46: X-ray reflectivity measurements between 2.25° and 6° performed while heating the sample over 210°C. A 2D surface plot (top) and a 3D Waterfall plot (bottom) is shown.

The crystal E peak at 3.2° vanishes together with all other peaks as shown in the long range measurement in figure 3.47. No smectic A phase is found.

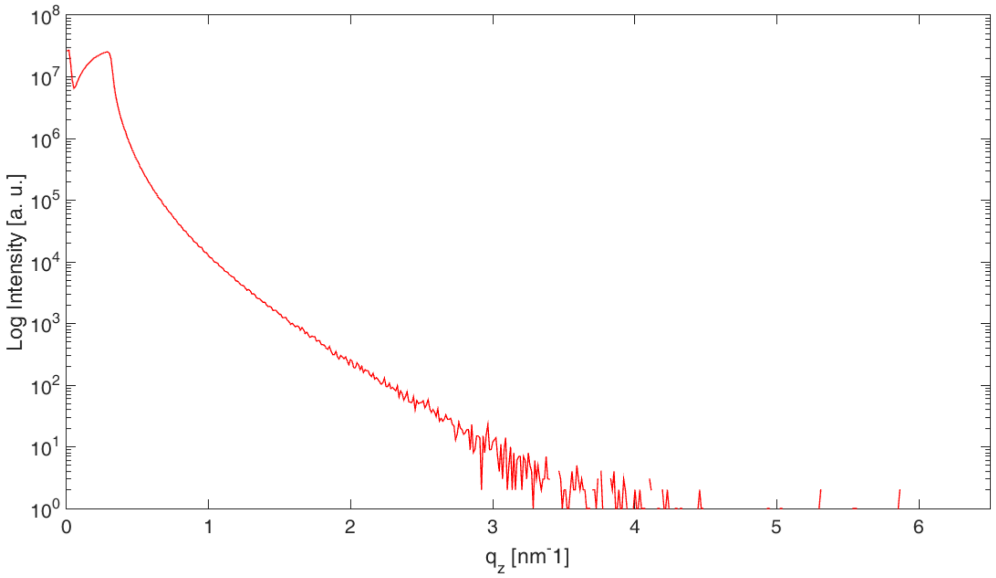

Figure 3.47: X-ray reflectivity measurement at 215°C showing no remaining peaks. All Bragg peaks vanished leaving behind the small Kiessig fringes of the SiO2 layer and the background signal.

When passing the melting point of 223°C and reducing the temperature again the peaks don't return. To investigate if a phase with Bragg peaks at higher angles is formed a specular measurement from 5° to 50° was performed. The curve is shown in figure 3.48. The visible peaks correspond to the substrate. The measurement confirms that there is no crystalline structure on the surface.

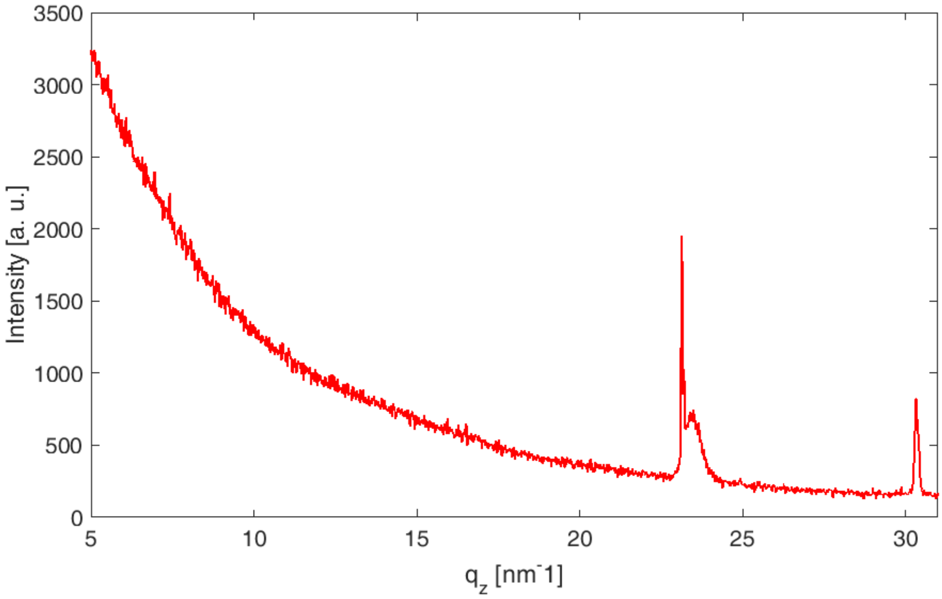

Figure 3.48: Specular X-ray diffraction measurement from q = 5 nm^{-1} to q = 32 nm^{-1} after temperature treatment over the melting point of 223°C and subsequent cooling to room temperature. All visible peaks correspond to the substrate.

The AFM picture in figure 3.49 (left) gives an insight to the surface structure. It shows smeared out material that might have been in a liquid phase at some point. However the height of the features is barely separable from the substrate and far below the long axis length of the molecule as described in the height distribution figure 3.49 (right).

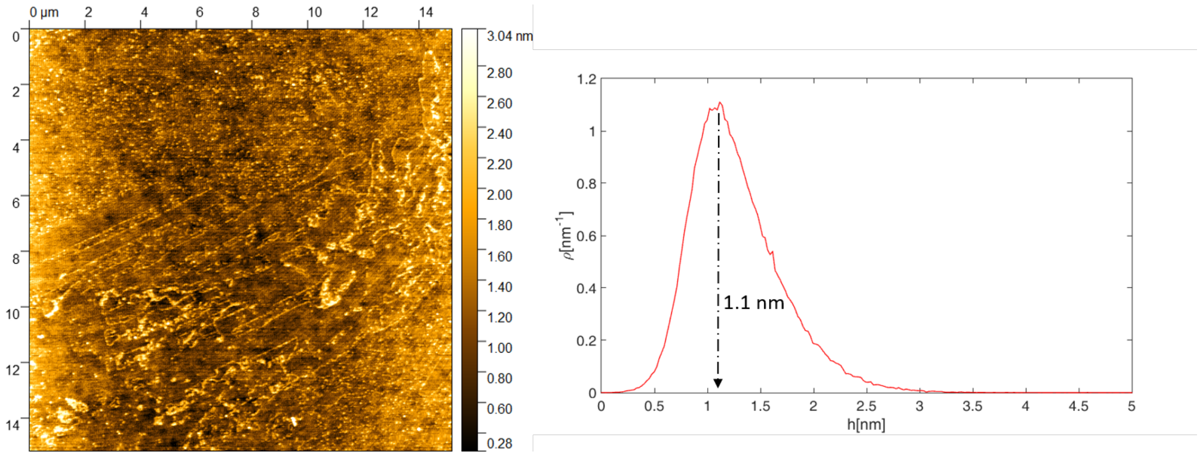

Figure 3.49: AFM measurement of a sample heated over the melting point and subsequently cooled down to room temperature (left) and the corresponding height profile of the picture. (right)

To understand the temperature behaviour of the mono- and multilayer structures they were thermally annealed using the DHS setup. The samples were brought to a temperature of 135°C within a few minutes and then slowly heated with a heating rate of 0.16°C per minute up to 155°C. Afterwards they were slowly cooled down with a cooling rate of 0.2°C per minute until reaching room temperature again. The monolayer dewetting structure that is present at a concentration of 0.3 g/l doesn't change significantly as shown in figure 3.50 in the AFM measurements.

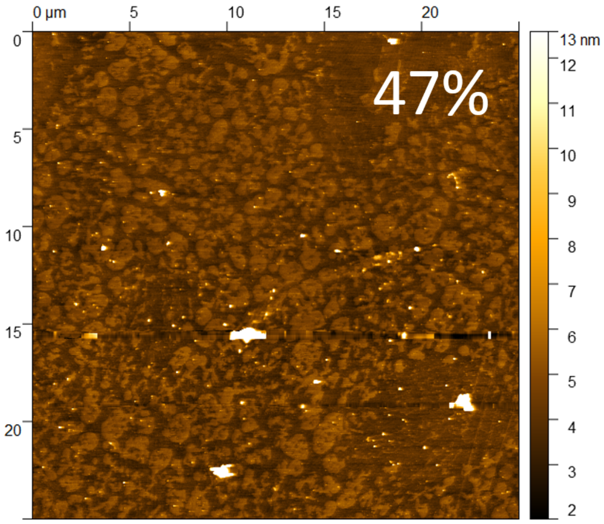

Figure 3.50: Atomic force microscope measurement of a sample that was thermally annealed at 155°C. The dewetting structure is maintained.

At higher concentrations of 0.5 g/l and 0.7 g/l where a multilayer structure is present temperature treatment has a strong effect. AFM measurements reveal that the first layer with the dendritic structure remains unchanged while the islands melt filling up the gaps between the dendrites. The coverage of the first layer increases. This suggests that the interaction between the molecules themselves from the first layer upwards is less thermally stable than the interaction between the substrate and the first layer. Furthermore, the observation at elevated temperatures that the molecules prefer to fill up the gaps between the dendrites rather than stay stacked upon each other indicates that the substrate-molecule interaction is stronger or more stable than the molecule-molecule interaction.

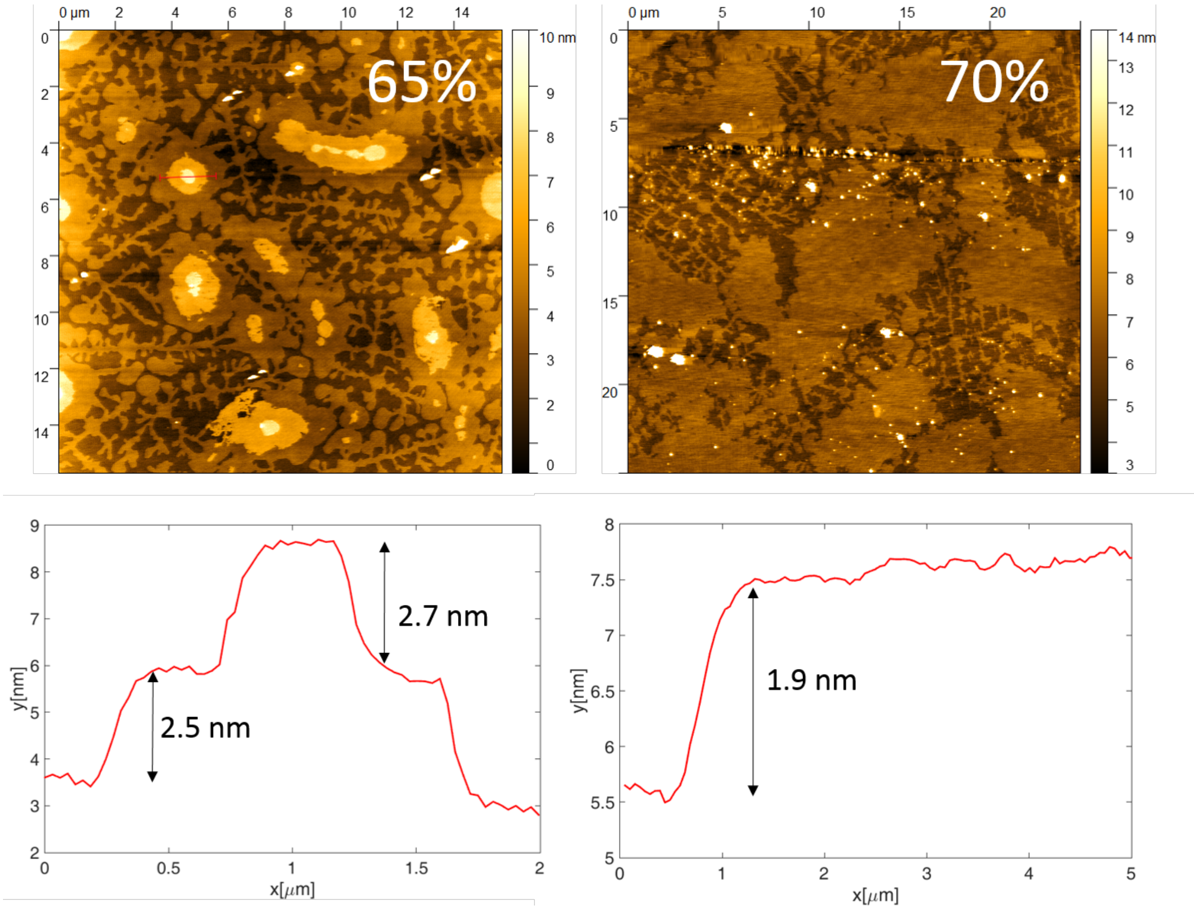

Figure 3.51: Atomic force microscope measurement of a sample that was temperature treated over the melting point of 223°C and subsequently cooled down to room temperature. The surface structure is shown (top) together with a height profile of the visible features (bottom).

In figure 3.52 the X-ray reflectivity measurements before and after annealing are shown. The Kiessig fringes get significantly bigger and start to resemble more a monolayer structure.

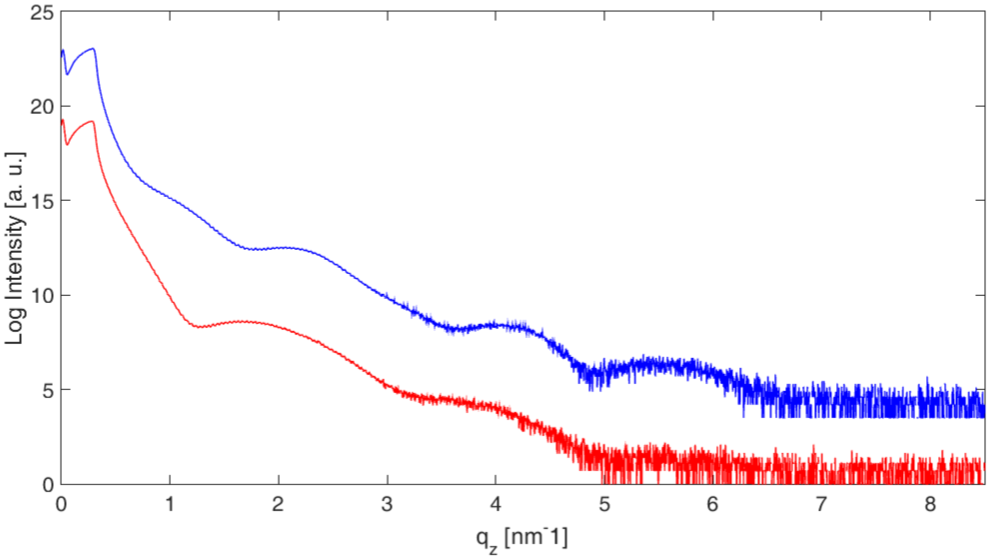

Figure 3.52: X-ray reflectivity measurements of a sample with a concentration of 0.5 g/l before (blue) and after (red) annealing.

The X-ray reflectivity fit of the annealed sample confirms the structure of the AFM measurements but again disagrees with the height as shown in figure 3.53 (bottom). Figure 3.53 (top) shows the reflectivity measurements of the annealed sample in comparison to a 0.3 g/l sample possessing a dewetting structure. The monolayer like shape of the data curve with two big fringes is stronger for the annealed sample. The fitting curves are indicated with the red lines and match the data very well. A two layer model as for all 0.3 g/l samples is used, one representing the lower dense alkyl chain and the other the more dense aromatic core of the molecule. Figure 3.53 (bottom) shows the resulting fitting parameters in comparison to the dewetting structure of a 0.3 g/l sample. The density value increases for the annealed sample. When multiplying the coverage of 70% to the expected aromatic core density of 1.4 g/cm^3 and the expected alkali chain density of 1 g/cm^3 we obtain 0.98 g/cm^3 and 0.70 g/cm^3 which is close to the values of the fit. The total height of both layers is 2.94 nm which is very close to the long axis molecular length.

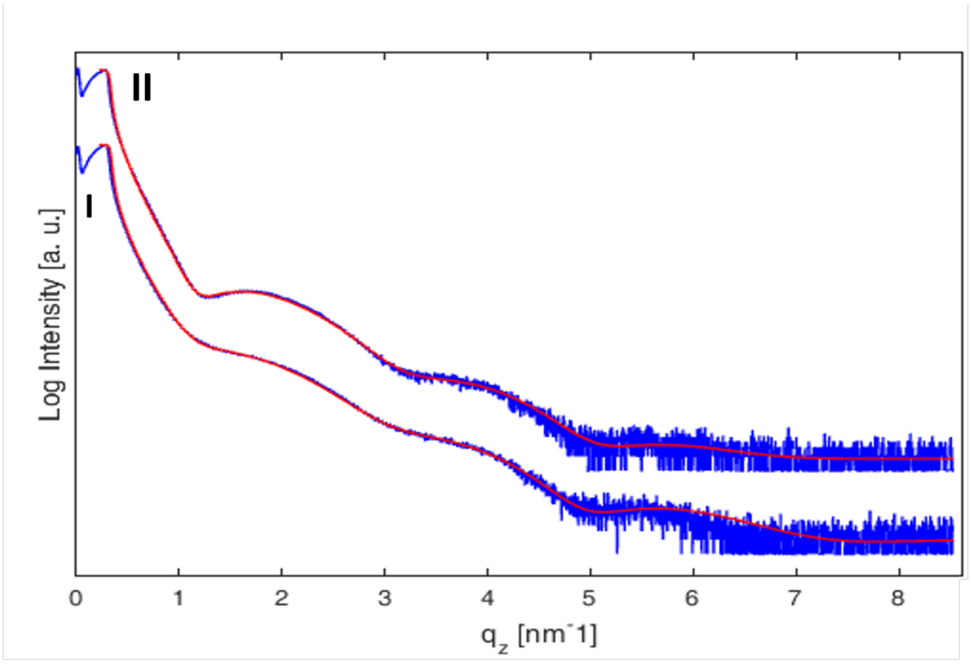

	I	II	
Layer 2	1,02	0,95	Tickness [nm]
	0,53	0,63	Density[g/cm^3]
Layer 1	2,00	1,99	Tickness [nm]
	0,7	0,89	Density[g/cm^3]

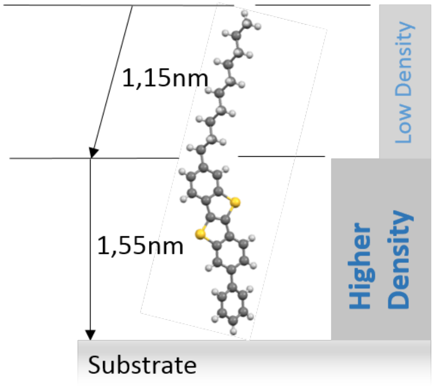

Figure 3.53: X-ray reflectively measurements (blue) together with their fits (red) for a sample prepared with a concentration of 0.3 g/l (I) and for a sample prepared with a concentration of 0.5 g/l and afterwards annealed (II).

4 Conclusion

4.1 Crystallization behavior

Ph-BTBT-10 shows different crystallization behaviours during spin coating depending strongly on the concentration of the solution and the spin speed. At low concentrations between 0.3 g/l and 0.5 g/l dewetting structures are observed. The X-ray reflectivity fits suggest that they are formed by upright standing molecules with the aromatic core pointing towards the substrate. At a concentration of 0.5 g/l and above, islands start to grow with terrace heights of the long molecular axis length according to the AFM measurements. The islands are connected by dendritic structures at the substrate surface. According to AFM measurements the dendrites possess a reduced height compared to the long molecular axis length of the molecule. The same is observed for AFM measurements at 0.3 g/l. This can be explained by a difference in cantilever-surface interaction when passing from the stiff substrate to the soft organic film. At concentrations above 2 g/l micrometer big crystals are formed that lead to the observation of bulk crystalline Ph-BTBT-10 Bragg peaks in the XRR measurements. The bulk crystal structure grows with the 001 surface parallel to the substrate. A disordered crystal E phase is producible at concentrations and spin speeds between 1.5 - 5 g/l and 1000 - 1600 rpm. This phase shows the same Bragg peak positions as the crystal E phase above 149°C, however the peaks are much broader suggesting a disordered phase.

4.2 Heat treatment

Heating experiments demonstrate a phase transition from the bulk crystalline phase to the crystal E phase at 149°C. Compared to the specular measurement of the bulk crystal phase every second Bragg peak starting from the 001 disappears. This corresponds to a inter planar distance of 2.6 nm and represents the long molecular axis length. It suggests that the molecules stack perpendicular to the surface onto each other without forming a bulk crystal structure. The transition is reversible when cooling back down and occurs at 103°C. After passing the melting point over 220°C and cooling back down no smectic A phase was found and no recrystallization occurs. No remaining material could be traced. The crystal E phase at over 149°C is quenchable into room temperature. When afterwards reheating the sample the bulk crystal structure returns at around 100°C. Heat treatment of the disordered crystal E phase samples confirm from two observations that they are in a crystal E like phase. The bulk peaks grow below 130°C just like for the quenched crystal E samples. Above 149°C the bulk peaks disappear again showing a very similar structure like before heating. A very striking observation for all heating experiments is that the peaks maintain their widths during the phase transitions. This suggests that the temperature increase supplies sufficient energy to provoke a reorientation into the new phase but insufficient for macroscopic structural change. Furthermore it implies that the phase transitions are driven by small local reorientation movements rather then drastic structural change.

Bibliography

[1] Jean-Luc Bredas, David Beljonne, Veaceslav Coropceanu, and Jerome Cornil. Charge-transfer and energy-transfer processes in π-conjugated oligomers and polymers: a molecular picture. *Chemical reviews*, 104(11):4971–5004, 2004.

[2] Hyunjoong Chung and Ying Diao. Polymorphism as an emerging design strategy for high performance organic electronics. *Journal of Materials Chemistry C*, 4(18):3915–3933, 2016.

[3] Dietrich Demus, John W Goodby, George W Gray, Hans W Spiess, and Volkmar Vill. *Handbook of Liquid Crystals, Volume 2A: Low Molecular Weight Liquid Crystals I: Calamitic Liquid Crystals*. John Wiley and Sons, 2011.

[4] Ying Diao, Kristina M Lenn, Wen-Ya Lee, Martin A Blood-Forsythe, Jie Xu, Yisha Mao, Yeongin Kim, Julia A Reinspach, Steve Park, Alan Aspuru-Guzik, et al. Understanding polymorphism in organic semiconductor thin films through nanoconfinement. *Journal of the American Chemical Society*, 136(49):17046–17057, 2014.

[5] S Diele, S Tosch, S Mahnke, and D Demus. Structure and packing in smectic e and smectic a phases in the series of 4-n-alkyloxy-4-alkanoylbiphenyls. *Crystal Research and Technology*, 26(6):809–817, 1991.

[6] Ahu Guemrah Dumanli and Thierry Savin. Recent advances in the biomimicry of structural colours. *Chemical Society Reviews*, 45(24):6698–6724, 2016.

[7] Hideaki Ebata, Takafumi Izawa, Eigo Miyazaki, Kazuo Takimiya, Masaaki Ikeda, Hirokazu Kuwabara, and Tatsuto Yui. Highly soluble [1] benzothieno [3, 2-b] benzothiophene (btbt) derivatives for high-performance, solution-processed organic field-effect transistors. *Journal of the American Chemical Society*, 129(51):15732–15733, 2007.

[8] Oumaima Gharbi. In-situ investigation of elemental corrosion reactions during the surface treatment of al-cu and al-cu-li alloys. 2016.

[9] Feng Huang. X-ray reflectively studies of thin films. *The University of Alabama, Tuscaloosa*, 2005.

[10] Hiroaki Iino, Takayuki Usui, and Jun-ichi Hanna. Liquid crystals for organic thin-film transistors. *Nature communications*, 6:6828, 2015.

[11] Takafumi Izawa, Eigo Miyazaki, and Kazuo Takimiya. Molecular ordering of high-performance soluble molecular semiconductors and re-evaluation of their field-effect transistor characteristics. *Advanced Materials*, 20(18):3388–3392.

[12] Andrew O. F. Jones, Basab Chattopadhyay, Yves H. Geerts, and Roland Resel. Substrate-induced and thin-film phases: Polymorphism of organic materials on surfaces. *Advanced Functional Materials*, 26(14):2233–2255.

[13] Andrew OF Jones, Yves H Geerts, Jolanta Karpinska, Alan R Kennedy, Roland Resel, Christian Roethel, Christian Ruzi, Oliver Werzer, and Michele Sferrazza. Substrate-induced phase of a [1] benzothieno [3, 2-b] benzothiophene derivative and phase evolution by aging and solvent vapor annealing. *ACS applied materials and interfaces*, 7(3):1868–1873, 2015.

[14] Oana D Jurchescu, Devin A Mourey, Sankar Subramanian, Sean R Parkin, Brandon M Vogel, John E Anthony, Thomas N Jackson, and David J Gundlach. Effects of polymorphism on charge transport in organic semiconductors. *Physical Review B*, 80(8):085201, 2009.

[15] Martin Kaltenbrunner, Tsuyoshi Sekitani, Jonathan Reeder, Tomoyuki Yokota, Kazunori Kuribara, Takeyoshi Tokuhara, Michael Drack, Reinhard Schwoediauer, Ingrid Graz, Simona Bauer-Gogonea, et al. An ultra-lightweight design for imperceptible plastic electronics. *Nature*, 499(7459):458, 2013.

[16] Shintaro Kobayashi and Katsuhiko Inaba. X-ray thin-film measurement techniques. *mass spectroscopy equipped with a skimmer-type interface*, page 8, 2012.

[17] Kazunori Kuribara, He Wang, Naoya Uchiyama, Kenjiro Fukuda, Tomoyuki Yokota, Ute Zschieschang, Cherno Jaye, Daniel Fischer, Hagen Klauk, Tatsuya Yamamoto, et al. Organic transistors with high thermal stability for medical applications. *Nature communications*, 3:723, 2012.

[18] Christoph Lercher. Surface induced polymorphism of dioctyl-terthiophene on silicon oxide. *Master's thesis, Graz University of Technology*, 2013.

[19] Hiromi Minemawari, Jun'ya Tsutsumi, Satoru Inoue, Toshikazu Yamada, Reiji Kumai, and Tatsuo Hasegawa. Crystal structure of asymmetric organic semiconductor 7-decyl-2-phenyl[1]benzothieno[3,2- b][1]benzothiophene. *Applied Physics Express*, 7(9):091601, 2014.

[20] Toru Mitsunaga. X-ray thin-film measurement techniques. *Rigaku J*, 25:7–12, 2009.

[21] Takahito Miyazawa, Yasuhisa Yamamura, Mafumi Hishida, Shigenori Nagatomo, Maria Massalska-Arodz, and Kazuya Saito. Revisiting smectic

e structure through swollen smectic e phase in binary system of 4-nonyl-4-isothiocyanatobiphenyl (9tcb) and n-nonane. *The Journal of Physical Chemistry B*, 117(27):8293–8299, 2013.

[22] Kazuki Niimi, Shoji Shinamura, Itaru Osaka, Eigo Miyazaki, and Kazuo Takimiya. Dianthra [2, 3-b: 2, 3-f] thieno [3, 2-b] thiophene (datt): Synthesis, characterization, and fet characteristics of new π-extended heteroarene with eight fused aromatic rings. *Journal of the American Chemical Society*, 133(22):8732–8739, 2011.

[23] Lyman G Parratt. Surface studies of solids by total reflection of x-rays. *Physical review*, 95(2):359, 1954.

[24] Roland Resel, E Tamas, Bernhard Sonderegger, P Hofbauer, and J Keckes. A heating stage up to 1173 k for x-ray diffraction studies in the whole orientation space. *Journal of applied crystallography*, 36(1):80–85, 2003.

[25] Frank Schreiber and Alexander Gerlach. X-ray and neutron reflectivity for the investigation of thin films. *Website: www.physchem.ox.ac.uk/fs*.

[26] Dieter Schwarzenbach. *Crystallography*. Wiley, 1996.

[27] Guillaume Schweicher, Vincent Lemaur, Claude Niebel, Christian Ruzie, Ying Diao, Osamu Goto, Wen-Ya Lee, Yeongin Kim, Jean-Baptiste Arlin, Jolanta Karpinska, et al. Bulky end-capped [1] benzothieno [3, 2-b] benzothiophenes: Reaching high-mobility organic semiconductors by fine tuning of the crystalline solid-state order. *Advanced Materials*, 27(19):3066–3072, 2015.

[28] Hans-Georg Steinruck, Andreas Schiener, Torben Schindler, Johannes Will, Andreas Magerl, Oleg Konovalov, Giovanni Li Destri, Oliver H Seeck, Markus Mezger, Julia Haddad, et al. Nanoscale structure of si/sio2/organics interfaces. *ACS nano*, 8(12):12676–12681, 2014.

[29] Kazuo Takimiya, Hideaki Ebata, Katsuhiro Sakamoto, Takafumi Izawa, Tetsuo Otsubo, and Yoshihito Kunugi. 2, 7-diphenyl [1] benzothieno [3, 2-b] benzothiophene, a new organic semiconductor for air-stable organic field-effect transistors with mobilities up to 2.0 cm2 v-1 s-1. *Journal of the American Chemical Society*, 128(39):12604–12605, 2006.

[30] Terence L Threlfall. Analysis of organic polymorphs. a review. *Analyst*, 120(10):2435–2460, 1995.

[31] Mahendra Kumar Trivedi, Alice Branton, Dahryn Trivedi, and Gopal Nayak. Isotopic abundance analysis of biofield treated benzene, toluene and p-xylene using gas chromatography-mass spectrometry (gc-ms). 2015.

[32] Oliver Werzer, Babara Stadlober, Anja Haase, H-G Flesch, and Roland Resel. Evaluation of organic sub-monolayers by x-ray based measurements under gracing incident conditions. *The European Physical Journal-Applied Physics*, 46(2), 2009.

[33] P. Yimsiri and M.R. Mackley. Spin and dip coating of light-emitting polymer solutions: Matching experiment with modelling. *Chemical Engineering Science*, 61(11):3496 – 3505, 200.

[34] Makoto Yoneya. On the monolayer crystal structure of the organic semiconductor 7-decyl-2-phenyl [1] benzothieno [3, 2-b][1] benzothiophene. *The Journal of Physical Chemistry C*, 2018.